Starch modified hyperbranched polyurethane/carbon dot-silver nanocomposite

Highlight

This chapter depicts the development of a bio-based smart implantable material with multifaceted attributes of high performance, potent biocompatibility and inherent antibacterial property, particularly against drug resistant bacteria, in biomedical domain. The chapter addresses these aspects at the bio-nano interfaces and describes the *in situ* fabrication of starch modified hyperbranched polyurethane (HPU) nanocomposites by incorporating different weight percentages of carbon dot-silver nanohybrid during polymerization process. This nanohybrid and its individual nanomaterials (Ag and CD) were prepared by facile hydrothermal approaches and characterized by various instrumental techniques. The nanocomposites exhibited significant improvement in the performance in terms of mechanical and thermal with 5 wt% of nanohybrid. They also showed notable shape recovery and nearly complete self-expansion just within 20 s at (37 ± 1) °C. Biological assessment established *in vitro* cytocompatibility of the HPU nanocomposites. Significantly, the antibacterial potency of the nanocomposites against *Escherichia coli* MTCC40 and *Staphylococcus aureus* MTCC3160 bacterial strains vouched for their application to countercheck bacterial growth, often responsible for biofilm formation. Thus, the nanocomposites have the potential to be used as tough infection-resistant rapid self expandable stents for possible endoscopic surgeries.

Parts of this work are published in

Duarah, R., Singh, Y. P., Gupta, P., Mandal, B. B., and Karak, N. High performance bio-based hyperbranched polyurethane/carbon dot silver nanocomposite: a rapid self-expandable stent. *Biofabrication,* 8:045013, 2016.

3.1. Introduction

The development of biocompatible and biodegradable starch modified hyperbranched polyurethane(s) (HPU) as thermoresponsive shape memory polymer(s) (SMP) was discussed in **Chapter 2**. Such bio-based SMP as implant devices can incorporate shape-memory effect at body temperature to trigger shape change after insertion into the human body for endoscopic surgeries, and biocompatibility to prevent bacterial adhesion [1-3]. In this milieu, thermally-induced SMP could also serve as another desired application namely, the eco-friendly stent with self-expandability attribute. However, contrary to commercial metallic stents which often cause various long-term side effects of infection, restenosis and thrombogenesis, a bio-based polymeric self-expandable stent offers a physical barrier to the vessel wall and presents a pharmacological approach in the prevention of thrombus formation and intimal proliferation [4, 5]. Tamai *et al.* developed a self-expandable poly(L-lactic acid) (PLLA) stent (the Igaki-Tamai stent) which achieved self-expansion at 70 °C by a heated balloon, and may likely induce vessel injury and trauma to the cells during deployment [6]. Venkatraman *et al.* developed a bilayered biodegradable self-expandable stent which achieved full expansion in minimum time of about 8 min under aqueous environment [7]. The known biodegradable chitosan based stent achieved self-expansion to about 50% over its initial diameter within a period of 3 min after insertion [8]. However, the self-expansion time of stents ought to be preferably less than a minute since rapid self-expansion favors the *in vivo* deployment and impede migration after insertion at the targeted region in the body [9]. Thus, a polymeric nanocomposite requires the incorporation of a suitable biocompatible nanomaterial which may impart strong interaction with the smart polymer matrix and thereby facilitate faster self-expansion, ideally to less than a minute to prevent the migration of the device during *in vivo* deployment.

Again, structural stability and mechanical strength are the essential properties of self-expandable polymeric stents to meet the basic biomedical norms. Implanted polymers commonly suffer from gradual loss of mechanical properties after initiation of the degradation process that can lead to the worst condition of fatigue failure [10]. To combat such difficulties of polymeric self-expandable stents, nanocomposites of SMPs have been projected where additions of a minute proportion of carbonaceous nano-particles in the formulation of the SMP matrix help elevate the diverse material performance [11]. In this regard, carbon dot(s) (CD) garnered extensive attention in

biomedical applications owing to their excellent nano-state aqueous solubility, dramatic optical properties and enhanced biocompatibility [12]. The aromatic carbon rich structure of CD with highly polar peripheral groups confers a strong physicochemical interaction with the polymer matrix to enhance the mechanical properties of the nanocomposite [13]. Further, with the potential for biomedical applications, CD serves as a suitable candidate for the development of a sustainable and biocompatible self-expandable stent. However, literature remains silent on the use of CD in a self-expandable stent system.

Further, biofilm formation on the inner surface of the stent is generally found after a certain period of its application, which may lead to stent blockage by bacterial colonization and in turn cause health complications due to malfunctioning of the stent [14]. Unfortunately, literature cited very few reports on infection-resistant stents. Gwon *et al.* evaluated the antibacterial effects of cefotaxime-eluting covered self-expandable stents in a canine biliary model and concluded that cefotaxime did not prevent biofilm development in a canine biliary [15]. Thus, development of an infection-resistant stent is the need of hour to address the issues of biofilm formation. In this context, silver nanoparticle(s) (AgNP) dominates the biomedical field for infection-resistant materials due to its broad range of potent antibacterial activity that prevents biofilm formation as reported in the literature [16, 17]. In 2015, Wen *et al.* designed polyurethane (PU) biliary stents modified with AgNP. Although *in vivo* experiments in pig models confirmed reduced bacterial adhesion on the stent, an inflammation was observed in the common bile duct and the abdominal cavity surrounding it [18]. On the other hand, Yang *et al*. developed an antibacterial plastic biliary stent coated with AgNP which exhibited poor mechanical performance [19]. Therefore, to address the shortcomings of poor mechanical property and to prevent bio-film formation of the polymeric self-expandable stents, use of a novel nanohybrid of CD and AgNP (CD-Ag) in such SMP system maybe the right proposition. This CD-Ag nanohybrid is expected to impart combined attributes of enhanced mechanical performance, thermal stability and improved biocompatibility to the proposed bio-based self-expandable stent. Thus, starch modified biodegradable HPU was used as a suitable matrix for the above smart nanocomposite. Moreover, no literature on starch based HPU/CD-Ag nanocomposites has been reported till date as a rapid self-expandable infection-resistant stent for biomedical applications.

In view of these facts, *in situ* fabricated starch modified HPU/CD-Ag nanocomposites as a high performing sustainable, tough infection-resistant rapid self-expandable stent was fabricated. The thermal responsive shape memory behavior,

physico-mechanical and thermal properties as well as *in vitro* hemocompatibility of mammalian red blood cell(s) (RBC) were investigated for the nanocomposites. Further, adherence and proliferation of smooth muscle cell(s) (SMC) and endothelial cell(s) (EC) were checked by *in vitro* study. The bacterial adherence of the fabricated nanocomposite films was studied by using bacterial strain. The prevention of biofilm formation by the fabricated nanocomposites against bacterial strains was also demonstrated. Furthermore, the performance of HPU/CD-Ag nanocomposite is also compared with HPU/CD and HPU/Ag nanocomposites to validate the superiority of the former for the same purpose.

3.2. Experimental

3.2.1. Materials

Polycaprolactone diol (PCL), Toluene diisocyanate (TDI), 1,4-butanediol (BD) and xylene of similar specifications and grade as described in **Chapter 2** (**Section 2.2.1**), were employed. DMAc (Merck, India) was vacuum-dried and stored with 4A-type molecular sieves overnight, prior to use. *Citrus limon* (*C. limon*) fruits were purchased from the local market at Tezpur, India. Hyperbranched starch modified polyol (HBSP) was prepared using the same method as described in **Chapter 2** (**Section 2.2.3.1**). Silver nitrate ($AgNO_3$, Sigma Aldrich, Germany) were used as received.

Moreover, nutrient broth (Himedia, India), nutrient agar (Himedia, India), heparin (Sigma Aldrich, USA), collagen (Sigma Aldrich, USA), phosphate buffered saline (PBS, pH 7.4, Hi-Media, India), neutral buffered formalin (NBF, Sigma Aldrich, USA), TritonX-100 (Sigma Aldrich, USA), rhodamine-phalloidin (1:40, Life Technologies, USA), lactate dehydrogenase (LDH) kit (Sigma Aldrich, USA), Dulbecco's Modified Eagle Medium (DMEM; Gibco), fetal bovine serum (FBS, Gibco), antibiotic-antimycotic solution (Himedia), ethidium homodimer (Sigma Aldrich, USA), Alamar Blue assay kit (Invitrogen, USA) were used in the biological evaluation of the HPU nanocomposite films.

3.2.2. Methods

3.2.2.1. Synthesis of CD from starch

CD was synthesized by a facile, economic and green one-step hydrothermal synthetic route using starch and lemon juice, without the addition of a base. In a typical procedure,

starch (5 g) was dissolved in 40 mL of distilled water, to which few drops of *C. limon* extract was added. Subsequently 20 mL of ethanol was added to the starch solution in an autoclave and heated for 5 h in an oven, at a steady temperature of 150 °C. On cooling to room temperature, a brown product was obtained which was dissolved in 20 mL water and then filtered to separate the residue. Finally, the solvent was evaporated at 60 °C under vacuum to obtain the water soluble dry CD with a yield of 54 mg mL^{-1}. In this study, bare CD was synthesized for the main purpose of demonstrating the biocompatibility effect of CD as well as its ability to act as a reinforcing material in the fabricated nanocomposites.

3.2.2.2. Preparation of AgNP

Citrus limon extract was prepared by squeezing the juice out of its fruits followed by filtration and centrifugation at 10,000 rpm for 10 min to remove any impurities. An amount of 40 mL of *C. limon* extract and 10 mL of 10^{-1} M $AgNO_3$ solution were mixed in the ratio of 4:1 to prepare the reaction mixture and stirred for 2 h at room temperature. The formation of AgNP was indicated by the color change from transparent to dark brown during the course of the reaction. After 2 h, the mixture was centrifuged at 10,000 rpm for 7-10 min to eliminate any uncoordinated aqueous soluble material. Thereafter, the AgNP were washed thrice with distilled water followed by acetone and finally dried in a vacuum oven at 50 °C. In this study, bare AgNP was synthesized to just demonstrate the effect of antibacterial activity in the prepared nanocomposites.

3.2.2.3. Synthesis of CD-Ag nanohybrid

CD-Ag nanohybrid was synthesized by the reduction of $AgNO_3$ solution by the *in situ* synthesized CD through a green one-step hydrothermal approach. An amount of 1.49 g of $AgNO_3$ was dissolved in 60 mL of distilled water and stirred for 15 min in a 100 mL beaker. Consequently, 3 g of starch in 40 mL water was taken in an autoclave and 20 mL ethanol was added to the above solution. The mixture was hydrothermally and continuously heated for 5 h at 150 °C. Subsequently, the solution was cooled to room temperature followed by centrifugation at 10,000 rpm for 10 min. Finally, the nanohybrid was washed with distilled water dispersed in it *via* sonication for 5 min.

3.2.2.4. Fabrication of HPU nanocomposites

PCL (6 g, 0.002 mol) and 0.36 g BD (0.36 g, 0.004 mol) were taken in a three necked round bottom flask which was equipped with a mechanical stirrer, an inlet for nitrogen gas and a Teflon septum. Minimum amount of xylene was added to facilitate stirring. After the total dissolution of PCL in xylene, TDI (0.007 mol, 1.22 g) was slowly added into the mixture at room temperature, followed by continuation of the reaction at (70 ± 2) °C, for 3 h. After the completion of the reaction, a viscous mass was obtained which was cooled to room temperature and considered as the pre-polymer.

Subsequently, hyperbranched polyol (1.4 g, 0.01 mol) was added to the pre-polymer as the branch generating moiety, with the remaining amount of TDI (0.35 g, 0.002 mol) in order to keep the NCO/OH ratio at unity. Gradually, the temperature was raised to (80 ± 2) °C and continuously stirred for 2 h and then the reaction mixture was cooled down to room temperature. A dispersion of CD-Ag nanohybrid in THF (1, 2 and 5 wt% of CD-Ag nanohybrid with respect to the total weight of HPU) was added to the reaction mixture and the temperature was slowly elevated to (80 ± 2) °C and made to run for 2 h for completion of the reaction, as affirmed by the disappearance of the isocyanate band at 2270 cm^{-1} in the FTIR spectrum [10, 20, 21]. Three separate polymerization reactions generate three *in situ* bio-based HPU/CD-Ag nanocomposites with 1, 2 and 5 wt% of CD-Ag, encoded as HPU/CD-Ag1, HPU/CD-Ag2 and HPU/CD-Ag5, respectively. Similarly, HPU/CD and HPU/Ag were also prepared using the same technique, except a dispersion of 1 wt% CD in DMAc and a dispersion of 1 wt% of AgNP in THF were added *in lieu* of CD-Ag, respectively, for comparison purposes. HPU was also prepared without the incorporation of any nanomaterial. All the nanocomposites were fabricated by the same *in situ* polymerization technique and hence some attributes of them were compared.

3.2.2.5. Sample preparation for performance study

HPU and its nanocomposite solutions were cast on glass slides (75 × 25 × 1.39) mm for gloss and scratch and steel strips (150 × 50 × 1.44) mm for impact studies, under the same conditions as mentioned in **Chapter 2**.

3.2.2.6. Antibacterial assay

Antibacterial assay was conducted against *Escherichia coli* (*E. Coli,* MTCC 40, Gram negative) and *Staphylococcus aureus* (*S. aureus,* MTCC 3160, Gram positive) to judge

the suitability of the material against the biofilm formation. Post culturing of the bacteria in nutrient broth for 6 h, the films of size (6 x 1) mm^2 were immersed in 1 mL of bacterial suspension culture and incubated at 37 °C. 100 µL of culture was withdrawn and analyzed spectroscopically at regular intervals. Visible turbidity and optical density (OD) of cultures were determined at 600 nm over a period of 5 h. Ampicillin (500 µg mL^{-1}) and gentamicin (500 µg mL^{-1}) were used as the positive control for the gram positive and gram negative bacteria respectively. All assays were performed in triplicate.

3.2.2.7. Bacterial adhesion test

The antibacterial activities of the polymeric films against *Pseudomonas aeruginosa* (*P. aeruginosa,* MTCC 1688, Gram-negative) were tested by FESEM to study bacterial adhesion to the films. *P. aeruginosa* were incubated with the films in 24-well tissue culture plates. The bacteria were streaked on plates containing nutrient agar and incubated at 37 °C until growing colonies reached desired sizes. For suspension culture inoculum, a single colony sample from the streak plate was collected with a sterile loop, added to nutrient broth, and incubated at 37 °C overnight. Bacterial cells from the overnight culture were diluted and seeded into individual wells of 24-well plates containing films (n = 3). Films without the bacteria were used as control. The plates were incubated at 37 °C under static conditions. After 12 h, samples were removed, washed twice with PBS and fixed with 2% glutaraldehyde. The samples were dehydrated with graded ethanol series and air dried. The samples were sputter-coated with gold and imaged under FESEM.

3.2.2.8. Platelet adhesion and LDH activity

Whole blood was collected from healthy porcine and blended with 5 U mL^{-1} heparin, to prevent clotting. Heparin primed blood was centrifuged at 3000 rpm for 10 min at 22 °C to obtain yellowish top layer of platelet rich plasma (PRP). Blood compatibility and anti thrombogenic capability of nanohybrid HPU films were assessed by looking into number of platelets adhered on surface as described elsewhere [22]. Circular discs (ϕ 6 mm) of films were incubated with 200 µL of PRP for 1 h at room temperature. Collagen (1.5 mg mL^{-1}) coated surface was used as a positive control. Post incubation, all films were washed twice with PBS (pH 7.4) and adhered platelets were fixed with NBF. Films were further treated with 0.1% (v/v) TritonX-100 for 15 min to permeabilize adhered platelets and stained with rhodamine-phalloidin (1:40).

In order to quantify the activated platelets adhering on to the films; LDH activity was measured [22]. PRP was incubated with films in a similar fashion as described earlier and adhered platelets were lysed with 1% TritonX-100 for 1 h at 37 °C. Platelet lysate was collected and centrifuged at 10,000 rpm in a cooling centrifuge at 4 °C to measure LDH activity. LDH kit was used to assess total LDH activity following manufacturer's protocol. LDH activity was reported as milliunits mL^{-1}. Amount of LDH was directly co-related with number of adhered platelets.

3.2.2.9. Hemolysis assay

Compatibility of the films with blood was used to quantify the amount of RBC lysis induced by test material as per previously reported protocols [23]. Whole blood was collected in heparin containing vial and centrifuged at 3000 rpm for 5 min at room temperature. Upper yellowish layer containing plasma was aspirated and discarded. RBC containing bottom layer was further washed with 150 mM NaCl buffer by repeated centrifugation. RBC containing blood was diluted 20 times with 150 mM NaCl buffer and 200 µL of diluted blood was incubated with HPU discs for 1h. For positive and negative control, 20% Triton-100 and 150 mM NaCl buffer were used respectively. Intact erythrocytes were pellet down by centrifuging the film treated blood at 3000 rpm. Supernatant was read at 540 nm in the multiplate reader. Absorbance was directly co-related with RBC lysis and plotted for each sample.

3.2.2.10. Isolation of vascular cells and culture

For primary vascular cell isolation, portion of descending porcine aorta was procured from local slaughter house in sterile PBS (pH 7.4). SMC and EC were isolated according to previous report with slight modification [24]. In brief, associated fat layer was removed using sharp scissors and smooth tubular structure was attained. Outermost adventitial fibroblast layer was peeled off slowly and the remaining part was digested with 0.01% collagenase IA from *Clostridium histolyticum* (Sigma Aldrich, USA). Post 1 h treatment, EC were scraped off from the luminal surface and plated in DMEM, supplemented with 10% FBS and 1% antibiotic-antimycotic solution. Remaining part containing SMC was further digested with the same enzyme solution for 8 h and extracted cell suspension was cultured in DMEM media. Cells were maintained in a humidified CO_2 incubator at 37 °C and 5% CO_2 level. Media was changed every

alternative day. Cells were passaged repeatedly and used between passage 3 and passage 8 for further experiments.

3.2.2.11. In vitro cytocompatibility study

In vitro compatibility of the films was evaluated by live/dead assay and Alamar Blue assay for viability and proliferation respectively [25]. Confluent porcine SMC and EC were trypsinized and suspended in DMEM supplemented with 10% FBS and 1% antibiotic-antimycotic solution. The films (6 x 1) mm were sterilized using 70% v/v ethanol for 2 h, washed with sterile PBS (pH 7.4) to remove residual alcohol and preconditioned with DMEM for 24 h before cell seeding. Seeding density and experiment time points for both cell types were kept the same to facilitate comparison of the results between the two cell types. Live/dead assay was performed using solution containing 4 mM calcein AM (for live cells) and 2 mM ethidium homodimer (for dead cells), according to manufacturer's protocol. Briefly, the cell-seeded films were rinsed with PBS (pH 7.4) and incubated with live/dead solution for (15-20) min at 37 °C in humidified incubator. Excess dye was washed with PBS and cells were visualized under florescent microscope. A cell seeded on tissue culture plate (TCP) was used as the control. Equal numbers of cells ($\sim 2x10^4$) were seeded on each film and the proliferation was assessed using Alamar blue assay kit on day 1st, 5th and 7th following the manufacture's protocol. Briefly, the cell-seeded films were incubated in medium containing 10% (v/v) Alamar blue dye for 3 h at 37 °C in a 5% CO_2 incubator. Post incubation, 100 µL media containing dye was withdrawn and read at 570/600 nm using multiplate reader. All assays were performed in triplicate.

3.2.2.12. Statistical analysis

All the experiments were performed at least in triplicates (n = 3) and the values are expressed as mean ± standard deviation. One way ANOVA was performed using Microcal OriginPro 8 to determine statistical significance. *$p \leq 0.05$ was considered significant and **$p \leq 0.01$ as highly significant.

3.2.2.13. Shape memory study

To study the shape-memory behavior of HPU and its nanocomposites, strip samples were heated at 70 °C (~T_m + 20 °C) for 5 min and transformed into a spiral shape. Immediately, the spiral samples were immersed in an ice-water salt bath at -(15 ± 5) °C

for 10 min to fix the temporary shape. The shape fixity of the cooled films was observed by drying them under vacuum followed by placing at room temperature (25 °C) for 30 min. Consequently, the fixed films were placed in a water bath at (37 ± 1) °C, during which shape recovery and the time required to retain original shape was noted. The shape recovery and shape fixity were calculated from the subsequent equations:

$$\text{Shape recovery (\%)} = [(90-\theta)/90] \times 100 \quad \text{(Eq. 3.1)}$$

$$\text{Shape fixity (\%)} = [\theta/90] \times 100 \quad \text{(Eq. 3.2)}$$

Where θ (degree) = the angle between the tangential line at the midpoint of the film and the line connecting the midpoint and the end of the curved film. The results are consistent as the test is repeated for five times [1, 20, 21]

3.2.2.14. Self-expandable study

To study the self-expandable behavior of HPU and its nanocomposites, strip samples with 10 cm in length and 0.5 cm in width were heated at 70 °C for 15 min and tightly wound on a cylindrical glass rod (5.00 mm in diameter), fixed by an adhesive tape and subsequently cooled down to -(15 ± 5) °C for 15 min. The outer diameter of the stent was measured as 5.43 mm after removal of the glass rod. The stent was then kept at room temperature for 30 min and its outer diameter was measured as 5.45 mm. Following the same procedure as above, the stent was then deformed and fixed on another cylindrical glass rod (diameter of 3.00 mm). Thereafter, the outer diameter of the stent before and after removing the mechanical force was measured as 3.43 mm and 3.45 mm, respectively. Finally, the stent was placed in a water bath at (37 ± 1) °C, and consequently change in its outer diameter was measured with the help of a vernier calliper.

3.2.3. Characterization

Fourier Transformed Infrared (FTIR) and X-ray diffraction (XRD) were used to characterize the nanomaterials and HPU nanocomposites, under the same conditions using the same instruments as stated in **Chapter 2** (**Section 2.2.2**). UV spectra of nanomaterials were recorded at room temperature (25 °C) using a Hitachi spectrophotometer (U2001, Tokyo, Japan). Electron Dispersive X-ray (EDX, Oxford, JSM-6390LV, UK) study was employed to confirm the elemental composition of the nanomaterials. The distribution of the nanomaterials within the polymer matrix as well as its size and shape were studied using High Resolution Transmission Electron

Microscopic (HRTEM) images acquired from JEOL, JEMCXII, Japan, microscope (operating voltage: 200 kV), using Cu grid of TED PELLA INC, Ultrathin C, Type A, 400 mesh. Using Gatan Microscopy Suite Software, the microscopic data was analyzed for Fast Fourier Transform (FFT) and Inverse Fast Fourier Transform (IFFT) images. TGA, DSC, UTM, scratch hardness tester, gloss meter, impact tester etc. were utilized as mentioned in **Chapter 2** (**Section 2.2.2**). The surface morphology of the nanocomposites was studied by a Field Emission Scanning Electron Microscope (FESEM, Zeiss, Sigma), after platinum coating on the surface. Fluorescently labelled platelets were imaged under a fluorescent microscope (EVOS FL, Life Technologies, USA). Multiplate reader (Tecan, Infinite M200, Switzerland) was used for the determination of the absorbance values in the hemolytic and Alamar Blue assays.

3.3. Results and discussion

3.3.1. Synthesis and characterization of CD

In 2012, the discovery of CD based nanoparticles in different carbohydrate based food caramels suggested the usefulness of CD for various biological applications, as the sources of extraction are standard food items and thus can be considered as safe and can be directly used for biological applications [26]. Moreover, the biocompatibility, *in vitro* cytocompatibility and low toxicity of CD against different cell lines make them promising candidates for biomedical applications [12, 13, 26]. Further, CD has the potentiality to promote biocompatibility of the nanocomposite system for allied biomedical applications [27].

In this study, CD was synthesized by hydrothermal acid hydrolysis of aqueous ethanolic solution of starch (containing carbohydrates like glucose, amylose and amylopectin) and citric acid as the carbon based bio-precursors *via* a facile, greener, one-step hydrothermal approach [28]. A plausible mechanism was projected for the formation of CD from starch and citric acid supported by reports on transformation of carbohydrates to carbon rich material (**Scheme 3.1**) [29, 30, 31]. In this study, carbohydrates are transferred to polymeric structure followed by graphitization. However, the carbonization process which resulted in 39.67% carbon (EDX data) and thus, is not a complete carbonization process, as it contains H and O. Initially, hydrolysis, dehydration and decomposition of starch took place in presence of citric acid,

resulting in soluble compounds (aldehydes, furfural etc.) and different organic acids (acetic acid, formic acid, etc.). The products are then transformed into soluble polymeric products on polycondensation, followed by their aromatization to result in aromatic clusters.

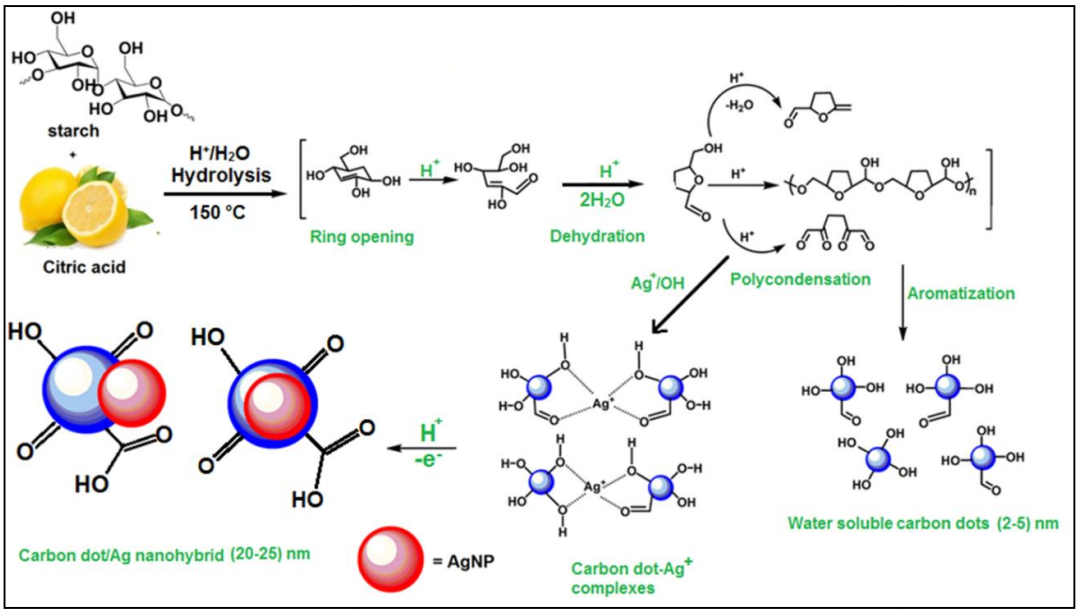

Scheme 3.1. Synthesis of CD and CD/Ag nanohybrid.

Thereafter, at a critical concentration there is a generation of huge amount of energy which results in the formation of water soluble CD [30, 31]. Hence, the reaction is promoted to occur under a relatively mild condition due to presence of glucose, amylose and amylopectin in starch. In the UV-visible spectrum of CD is shown in **Figure 3.1a**. An absorption peak at around 227 nm was observed, attributed to π-π* transition of the conjugated C=C band and an absorption peak at 282 nm (with a tail extending into the visible range), attributed to the n-π* transition of the C=O band. The XRD pattern of CD displays a broad peak near 21.1° corresponding to the (002) peak indicating that the interlayer of CD (0.42 nm) is higher than that of the graphitic interlayer spacing (0.33 nm) along with the characteristic broadness as shown in **Figure 3.1b** [27]. EDX spectrum (**Figure 3.1c**) confirmed the presence of C and O in weight and atomic ratios of 39.67:60.33 and 46.69:53.31, respectively. The polar functional groups and linkages in CD were evident from FTIR data. In the FTIR spectrum of CD in **Figure 3.1d**, the absorption frequencies at 3491, 2934, 1731, 1622, 1420, 1266 and 917 cm^{-1} confirmed

the presence of OH, C-H, C=O, C=C, C=O-C, C=O and an epoxy group, respectively, thus implying that the synthesized CD have remarkable water solubility [31]. The HRTEM images clearly depict the formation of almost spherical shaped CD with dimension in the range of (2.2-5.2) nm in **Figure 3.1e**.

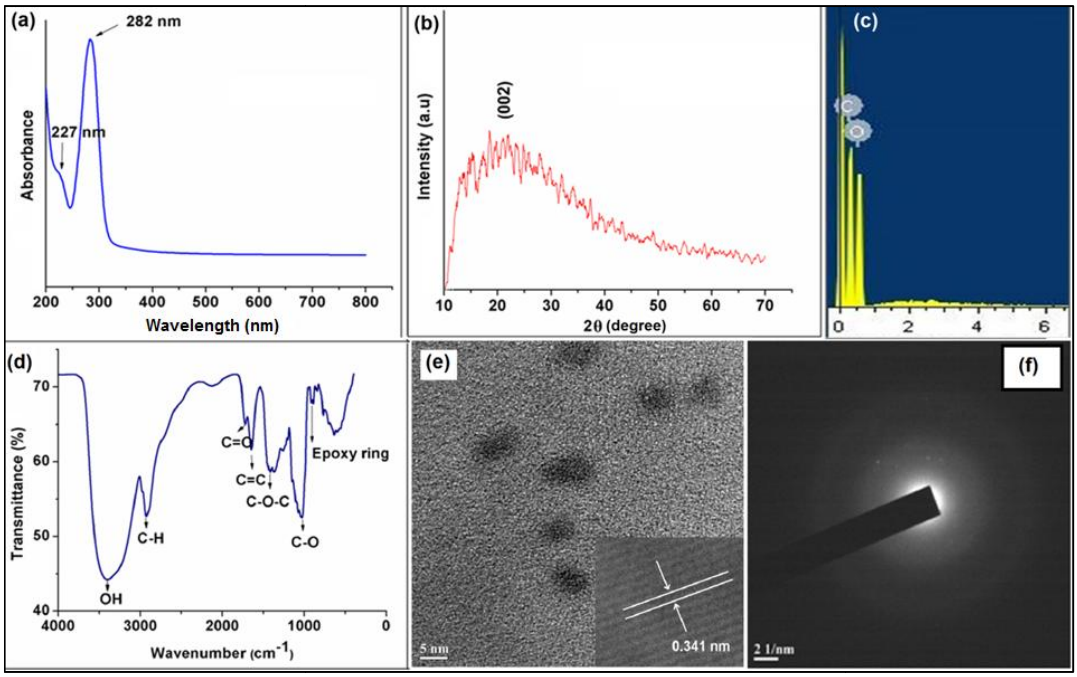

Figure 3.1. (a) UV absorption spectrum, **(b)** XRD pattern, **(c)** EDX map, **(d)** FTIR spectrum, HRTEM images at **(e)** 5 nm magnification with IFFT image (showing the lattice fringes) as inset and **(f)** SAED pattern of CD.

IFFT image ascertained the lattice spacing of 0.341 nm of the CD, which is close to the (002) lattice spacing of graphite, shown as inset of **Figure 3.1e** [27]. The poor crystalline nature of CD is attributed to the greater number of oxygen containing groups, as established from the selected area electron diffraction (SAED) pattern in **Figure 3.1f**, as well as the XRD pattern.

3.3.2. Preparation and characterization of AgNP

The addition of lemon extract (citric acid) to the $AgNO_3$ solution changes the color from pale yellow to dark brown which was deepened with time. The reduction of Ag^+ ions and the formation of AgNP occurred within an hour of reaction by the transition of electron(s) (e^-) from citric acid to Ag^+. The formation of AgNP was initially confirmed

from UV-visible spectroscopy by the Surface Plasmon Resonance (SPR) band in the range of (410-413) nm as shown in **Figure 3.2a** [32]. The EDX analysis in **Figure 3.2b** revealed the presence of a strong signal of Ag and confirmed the presence of AgNP. Signals of carbon and oxygen were also present apart from Ag, due to the residual presence of starch and lemon extract. The XRD pattern shows the formation of face centered cubic (fcc) Ag, confirmed by the peak positions at 2θ values (in degree) of 38.3, 44.5, 64.2 and 74.1 as presented in **Figure 3.2c**.

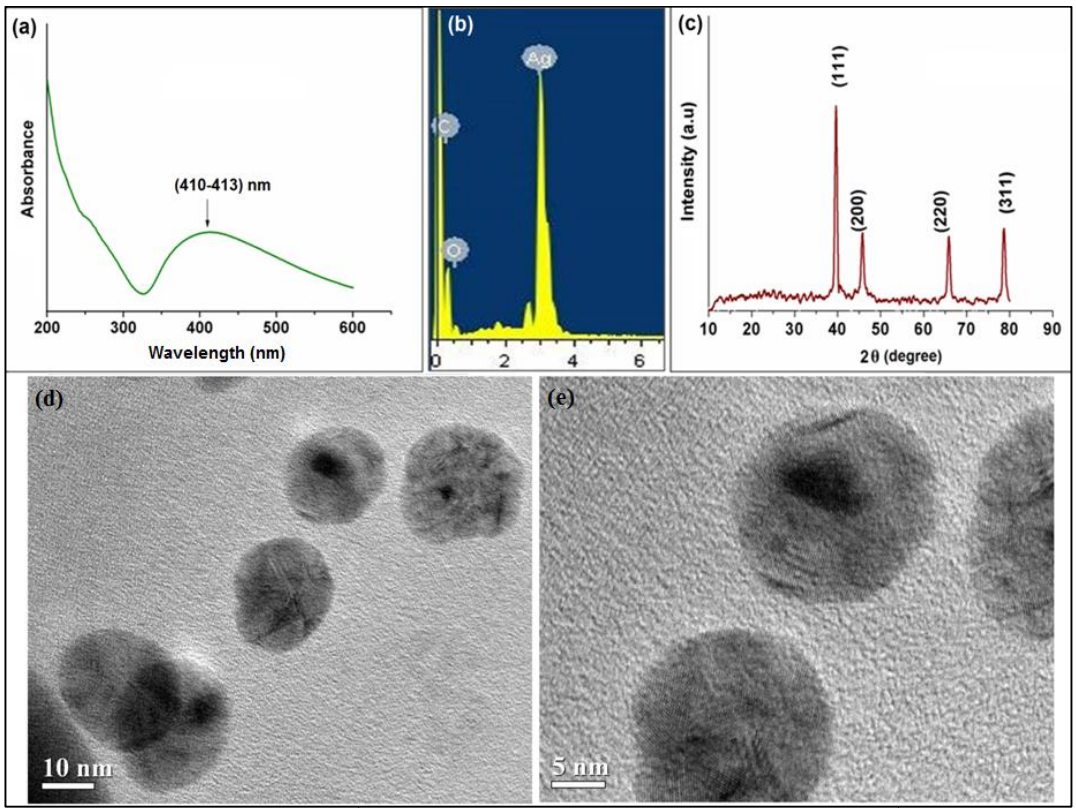

Figure 3.2. (a) UV absorption spectrum, **(b)** EDX map, **(c)** XRD pattern, **(d)** AgNP and **(c)** CD-Ag nanohybrid, and HRTEM images at magnifications **(d)** 10 nm and **(e)** 5 nm of AgNP.

These correspond to the characteristic Bragg's reflection planes (111), (200), (220) and (311), respectively (JCPDS 89-3722). The TEM analysis (**Figure 3.2d** and **e)** at different magnifications reveal that maximum particle density of AgNP was within (10-15) nm and no sign of agglomeration was observed. This affirms the stability of the synthesized nanoparticles, primarily observed through UV-visible spectroscopy.

3.3.3. Synthesis and characterization of CD-Ag nanohybrid

As mentioned earlier, CD was prepared by starch (carbon source) and citric acid *via* a one-step hydrothermal approach (**Scheme 3.1**). CD-Ag nanohybrid was also synthesized by the reduction of Ag^+ ions by the *in situ* synthesized CD through a one-step hydrothermal approach. The *as prepared* CD acts as a reducing agent in the preparation of AgNP owing to the presence of carbonyl, hydroxyl, carboxylic acid and epoxy groups on its surface. Mainly peripheral polar groups such as hydroxyl and aldehyde of CD help to reduce the Ag^+ into AgNP. In this case, Ag ions in the hydrothermal approach are reduced directly by transferring the e^- from CD as it contains large number of hydroxyl groups which can easily transfer e^- by polyphenolic mechanism. The CD not only serves as the reducing agent but also as the capping agent, in this reduction process. This is again attributed to the large number hydroxyl, carbonyl, carboxylic acid and epoxy groups present on the surface of CD, as reported earlier [27, 31]. The hydroxyl groups reduce Ag^+ by a polyphenolic mechanism, whereas the aldehyde groups reduce Ag^+ as in the Benedict reaction [28, 32]. It is pertinent to mention that the reduction of Ag^+ to Ag^0 under the presence of CD precursors cannot be ruled out completely. In addition, the composition of CD precursors like starch and lime extract has an abundance of citric acid, thiamin, riboflavin, niacin, carbohydrates, fats etc. These biomolecules have a number of surface hydroxyl groups, [28, 31] which can primarily reduce monovalent Ag and transform themselves to corresponding carbonyl group which was authenticated from the results obtained from the FTIR analysis. The FTIR spectrum of CD-Ag nanohybrid in **Figure 3.3a** shows that the amount of hydroxyl groups near (3400-3500) cm^{-1} of CD decreased and the amount of carbonyl groups (at 1650 cm^{-1}) increased after the formation of CD-Ag nanohybrid. This specifies that the hydroxyl and aldehyde groups of CD are transformed into keto and carboxylic acid groups after the formation of nanohybrid. The formation of CD-Ag nanohybrid was also confirmed from UV-visible spectroscopy in **Figure 3.3b** by a broad optical absorption peak near (227-280) nm, due to n-π* transition of the C=O band and π-π* transition of conjugated C=C band of CD, as well as SPR band of AgNP near 400 nm. There is a blue shift of the SPR band of AgNP in the range of (380-385) cm^{-1}, due to the reduction of size of Ag as it is generated *in situ* in CD where Ag ion forms complexes with OH and CO groups of CD and other precursors, present in the system. Thereby, the Ag^+ is embedded with the *in situ* generated CD which acts as the reducing agent as well as the capping agent in the prepared AgNP.

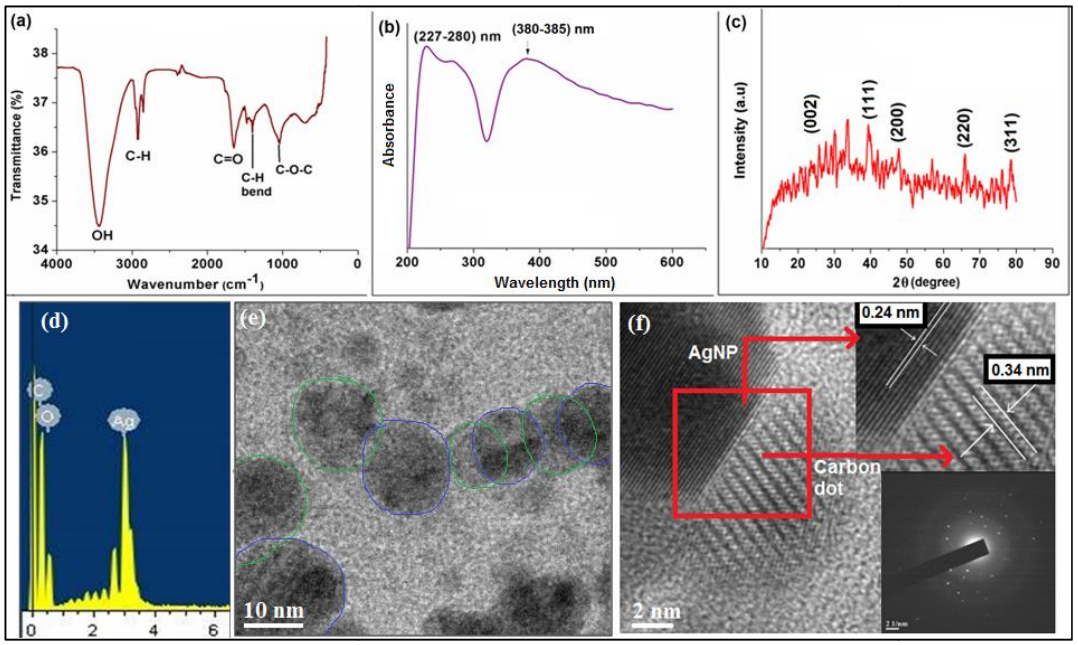

Figure 3.3. (a) FTIR spectrum, **(b)** UV absorption spectrum, **(c)** XRD pattern, **(d)** EDX map, and TEM images of CD (blue lines) and AgNP (green lines) at different magnifications **(e)** 10 nm and **(f)** 2 nm of the CD-Ag nanohybrid. The insets are an IFFT image (showing the lattice fringes) and SAED pattern of CD-Ag nanohybrid.

As the reduction in size of AgNP is significant in comparison to the system without CD, there is a considerable blue shift of the SPR band of AgNP in the UV absorption spectrum of CD-Ag nanohybrid. The XRD pattern of nanohybrid in **Figure 3.3c** shows the peaks of 2θ values (in degree) at 38.3, 44.6, 64.2 and 74.1 assigned to the (111), (200), (220) and (311) planes of face centered cubic (fcc) of AgNP. The broad peak of CD appears at 21.1° corresponding to (002) plane. EDX spectrum as shown in **Figure 3.3d** confirmed the presence of C, O and AgNP in the nanohybrid. The weight and atomic ratios of C, O and Ag in the nanohybrid were found to be 14.05:4.43:81.52 and 53.12:12.57:34.31, respectively. The HRTEM image in **Figure 3.3e** confirms the formation of nearly spherical AgNP (green border) embedded CD (green border) in the CD-Ag nanohybrid, held together by strong interactive forces that mutually stabilize each other. The diameter of AgNP embedded to CD in the nanohybrid is observed to be smaller (in the range of (6-8) nm) than that of the bare AgNPs (in the range of (10-15) nm). This is attributed to the fact that AgNPs are formed *in situ* in the CD by the formation of complexes with the OH and CO peripheral polar groups of the CD. This is further confirmed from the UV visible spectrum of CD-Ag nanohybrid where the SPR

band of AgNP underwent a blue shift, thus indicating the formation of smaller AgNP in the CD-Ag nanohybrid. Also, the size of CD in CD-Ag nanohybrid is found to be larger (in the range of (11-15) nm) than that of the bare CD. This may be attributed to the high surface energy of the particles, which induces agglomeration within them. Thus, the size of the nanohybrid is found to be in the range of (20-25) nm. The formation of a crystalline structure of CD-Ag nanohybrid with lattice spacing of 0.34 nm attributed to (002) plane of graphitic carbon and a well-defined crystal lattice of 0.24 nm in size for (111) plane of AgNP is clearly indicated from the IFFT image (showing the lattice fringes) and SAED pattern, shown as insets of **Figure 3.3f**.

3.3.4. Fabrication and characterization of HPU nanocomposites

The HPU nanocomposites were fabricated by incorporating CD, AgNP and CD-Ag as the nanomaterials (**Scheme 3.2**) in HPU matrix, separately. Here it is pertinent to mention that HPU/CD and HPU/Ag nanocomposites were prepared to demonstrate the biocompatibility and reinforcing effects of CD and antibacterial activity of AgNP, respectively, as already mentioned. The crucial factors for the successful preparation of HPU nanocomposites are concentration of the reactants, reaction time, rate of addition of the branching moiety and temperature [33]. In the second step of the reaction, the branching moiety was gradually added at room temperature, as a dilute solution (15-20% in xylene) in order to avoid gel formation. The nanomaterial was also incorporated in the second step of the reaction which interacted with some of the hydroxyl-terminated pre-polymer chains and imparted strong interfacial interactions, particularly with CD-Ag nanohybrid [1, 20]. Finally, the reaction temperature was slowly raised to (80 ± 2) °C and kept constant for the completion of the reaction. The FTIR spectra for HPU and its nanocomposites are shown in **Figure 3.4a**. Strong interfacial interactions result in better stabilization of nanoparticles within the matrix. A noteworthy alteration was observed in the region (1730-1685) cm^{-1} where HPU displayed a single band at 1730 cm^{-1}, but was split into two bands in the FTIR spectra of the nanocomposites [33, 34]. The bands in the region (1668-1685) cm^{-1} are mainly due to hydrogen bonding (H-bonding) interactions of the -C=O and -NH groups with AgNP while the functional groups of CD remained intact. Further, the intensity of the band at 1730 cm^{-1} for HPU/CD-Ag5 is less compared to the others may be due to greater wt% of nanomaterial. This is also supported by the shift of -NH absorption band from (3465 to 3455) cm^{-1} [32].

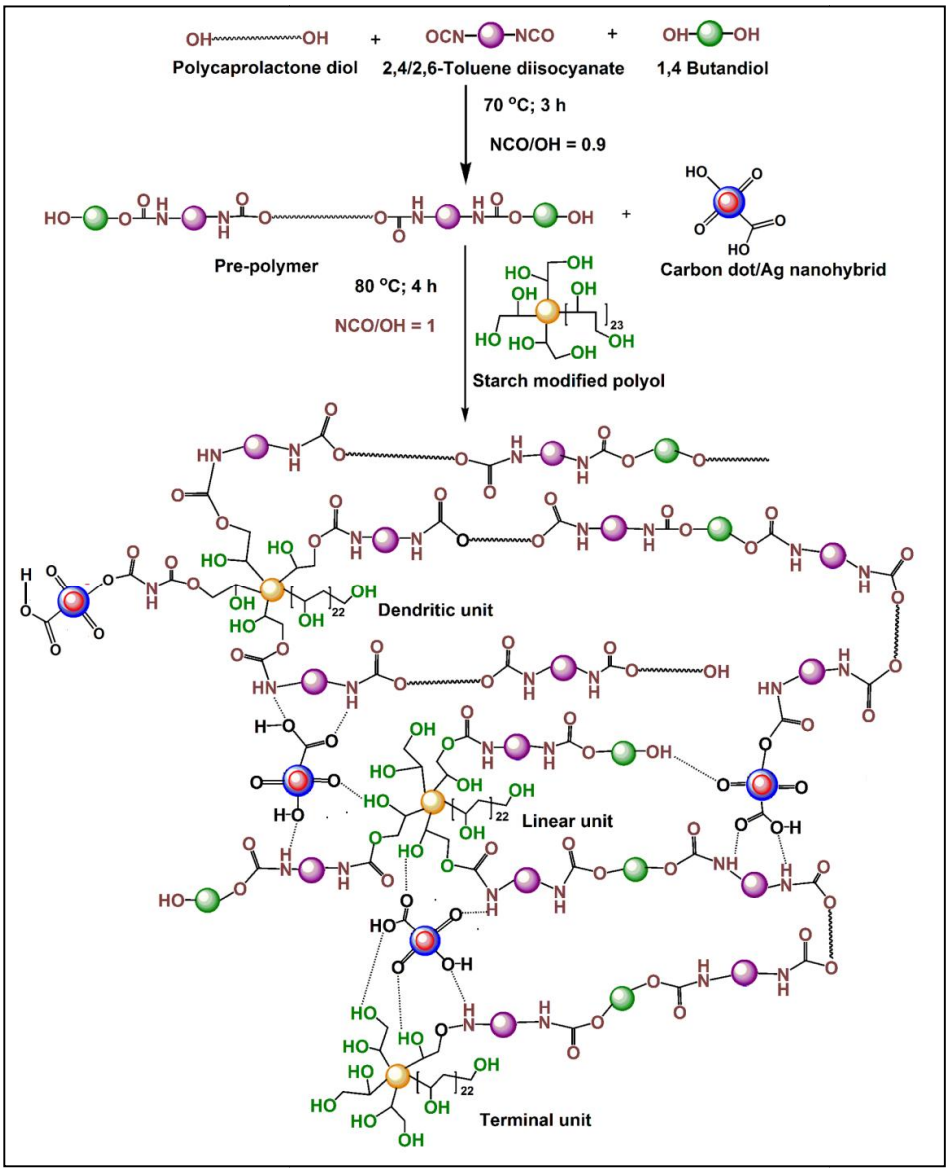

Scheme 3.2. Fabrication of HPU/CD-Ag nanocomposite.

Moreover, the disappearances of the isocyanate band at 2270 cm^{-1} clearly indicates that there is no free isocyanate in the system [1, 20]. The XRD patterns of HPU nanocomposites are shown in **Figure 3.4b**. HPU as well as its nanocomposites exhibited two distinct peaks at 2θ = 21.1° (d spacing = 4.19 Å) and 23.4° (d spacing = 3.81 Å), attributed to the crystalline PCL moiety present in the matrix [20]. The characteristic peak of CD at 21.1° in HPU/CD and HPU/CD-Ag nanocomposites may be masked by the highly intense PCL peaks. On incorporation of the nanomaterial, the PCL peaks shifted towards a higher angle which is attributed to the formation of a more dense structure as compared to the pristine HPU [33].

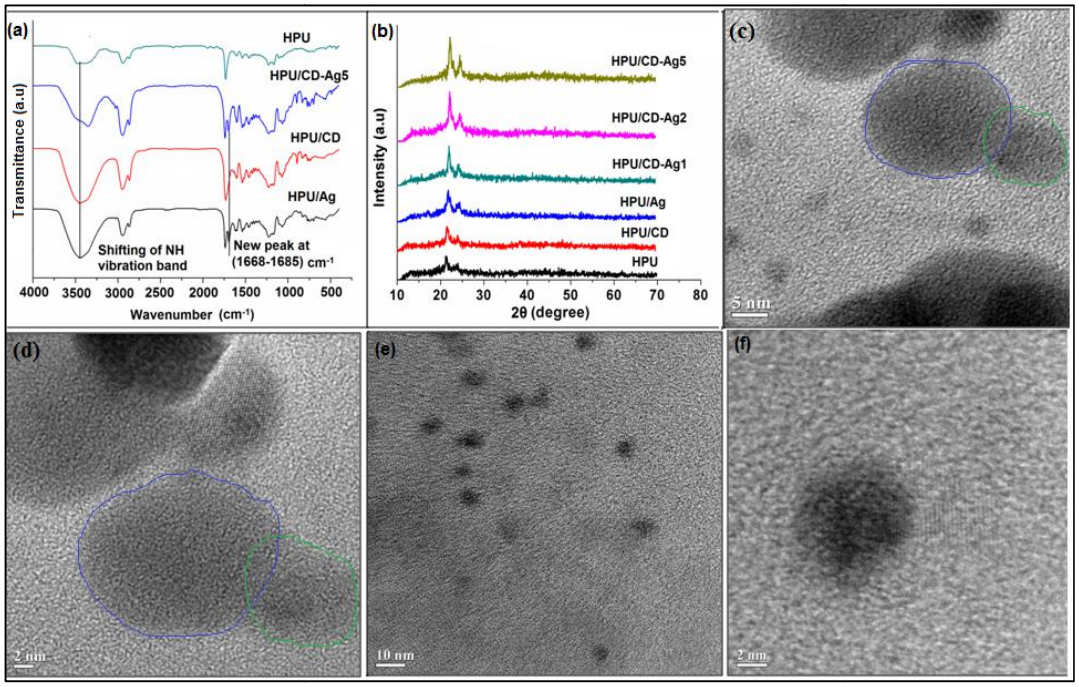

Figure 3.4. (a) FTIR spectra and **(b)** XRD patterns of HPU and its nanocomposites, and HRTEM images at magnifications **(c)** 5 nm and **(d)** 2 nm of HPU/CD-Ag5; and HRTEM images at magnifications **(e)** 10 nm and **(f)** 2 nm of HPU/CD.

This signifies the increased crystallinity of the nanocomposites with increase in the amount of nanomaterial which acts as a nucleating agent. With an increase in the amount of CD-Ag nanohybrid, the peak intensity of the PCL moiety also increased due to the strong nucleating effect of CD and an enhanced interaction of CD with the HPU matrix. However, no distinctive peak was observed for AgNP in the XRD patterns of the nanocomposites as a very small amount of AgNP was present in them. The performance of the HPU nanocomposites is significantly influenced by the dispersion of the nanomaterial in the HPU matrix and their interfacial interactions. Thus, HRTEM was used to study the dispersion of nanomaterial. The HRTEM images of HPU/CD-Ag5 in **Figure 3.4c** and **d** and HPU/CD nanocomposites in **Figure 3.4e** and **f** confirmed homogenous dispersion of the respective nanomaterial with the HPU matrix.

3.3.5. Mechanical properties

Generally, stent applications demand high strength, toughness and flexibility of the final article. Unfortunately, pristine polymeric material alone cannot offer adequate strength and bioactivity as a suitable load bearing prosthesis. To prevail over this difficulty,

fabrication of the polymeric materials with nanomaterial can endow them with favorable mechanical performance. The present investigation observed enhancement of mechanical performance of all the nanocomposites containing CD, Ag and CD-Ag nanohybrid. However, all three compositions of HPU/CD-Ag nanocomposites demonstrated much improved mechanical properties (tensile strength, toughness, elongation, impact resistance and scratch hardness) compared to HPU/CD and HPU/Ag nanocomposites (**Table 3.1**). This can be attributed to better dispersion of CD-Ag nanohybrid in the reaction medium compared to CD and AgNP independently. CD-Ag nanohybrid possesses varieties of polar oxygeneous and polar Ag-oxygen linkages which can interact with the HPU matrix either through secondary interactions or covalently, without agglomeration. The aromatic carbon rich structure of the CD in the CD-Ag nanohybrid imparts superior physicochemical interactions with the HPU matrix by virtue of its large peripheral polar functional groups.

Table 3.1. Mechanical properties of HPU and its nanocomposites

Property	**HPU**	**HPU/ Ag**	**HPU/ CD**	**HPU/ CD-Ag1**	**HPU/ CD-Ag2**	**HPU/ CD-Ag5**
Tensile strength (MPa)	17 ± 0.5	19 ± 0.3	23 ± 0.5	24.8 ± 0.5	26 ± 0.4	29 ± 0.4
Elongation at break (%)	1320 ± 4	1123 ± 2	1260 ± 3	1210 ± 5	1184 ± 8	1006 ± 4
Scratch hardness (kg)	6.5 ± 0.4	6.5 ± 0.3	7 ± 0.3	6.5 ± 0.2	7.5 ± 0.5	8.5 ± 0.4
Impact strength (kJ m^{-1})[a]	>19.02	>19.02	>19.02	>19.02	>19.02	>19.02
Toughness (MJ m^{-3})[b]	169 ± 2	176 ± 3	236 ± 2	243 ± 3	249 ± 2	251 ± 3

[a]*Maximum limit of the instrument.*

[b]*Calculated by integrating the area under stress-strain curves.*

Subsequently, this leads to significant improvement in strength and toughness of the fabricated nanocomposites. These strong H-bonding, covalent bonding, and polar-polar interactions between the nanohybrid and the HPU chains stiffen the hard segments of

HPU and facilitates the successful shift of the load from HPU matrix to the nanomaterial in the nanocomposite [1, 20, 33]. Thus, the tensile strength of the nanocomposites was greatly enhanced as shown in **Figure 3.5a**. The nanocomposites also confirmed an effective dose-dependent toughness subsequent to incorporation of the nanohybrid, HPU/CD-Ag5 and HPU/CD-Ag1 exhibited the highest and the lowest toughness, respectively.

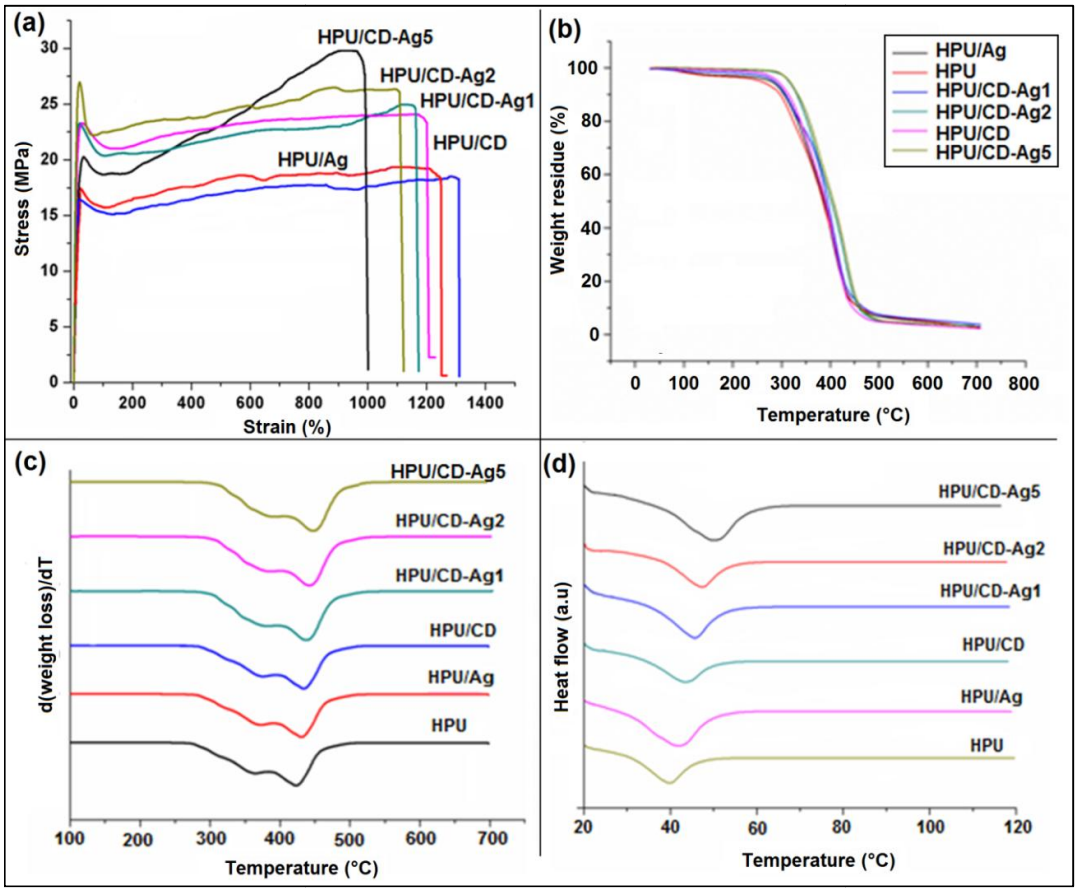

Figure 3.5. (a) Stress-strain profiles, **(b)** TGA thermograms, **(c)** DTG curves; and **(d)** DSC curves of HPU and its nanocomposites.

Interestingly, although HPU/CD-Ag1 contains half the amount of CD as compared to HPU/CD, the presence of an equal amount of AgNP in HPU/CD-Ag2 enhances its mechanical properties owing to the increase in interactions of AgNP with the hard segment of HPU matrix (confirmed from FTIR analysis) and enhanced crystallinity (as discussed under DSC). However, the HPU/Ag and HPU/CD-Ag nanocomposites exhibited a strong dose dependent diminution of elongation, compared to HPU, as the

incorporation of nanomaterial restricts the segmental motions of the polymer chains. In this regard, HPU/CD exhibited a higher elongation at break as compared to HPU/Ag owing to the presence of high polar peripheral groups (as evident by FTIR spectral analysis in **Figure 3.4a**) of the aromatic carbon rich structure of CD which confer a strong physico-chemical interaction with the HPU matrix. The excellent compatibility of CD with the HPU matrix serves in the proper alignment of the HPU chains during the initial stage of tensile loading and forces them to orient the multi layered graphitic structure (as evident by TEM infringes analysis in **Figure 3.3f**) in CD along the direction of loading. When a mechanical stress is applied on the nanocomposites, alignment of HPU chains along the direction of loading during initial stress and the sliding of the graphene layers over one another when attached to the polymeric chains during high stress contributes to the increased elongation. It is pertinent to mention that similar phenomenon was observed in RGO based polymeric system where both the strength and strain of the nanocomposites were enhanced due to the same mechanism [1, 33]. Thus similar phenomenon may arise in fabricated nanocomposites provided the nanomaterial can covalently link with the polymeric chain. In nutshell, the overall elongation at break for all the films was found to be very good. The scratch hardness was improved with the incorporation of nanomaterial into the HPU matrix. Also, the HPU nanocomposites exhibited the highest limit of impact energy owing to the presence of soft segments in the HPU chain, which dissipates the impact energy. Thus, overall mechanical performance of HPU/CD-Ag5 was found to be superior among the other known self-expandable stents and emphasizes the suitability of the former for applications of high load bearing self-expandable stent [2, 6, 7].

3.3.6. Thermal properties

Thermal study of HPU nanocomposites were conducted to study the degradation pattern using TGA as shown in **Figure 3.5b**. The nanocomposites exhibited a two-step degradation patterns due to the presence of both hard and soft segments in HPU matrix in **Figure 3.5c**. This suggests that the nature and load of the nanohybrid do not drastically control the degradation mechanism of the nanocomposites. All the nanocomposites exhibited particularly higher thermal stability as compared to HPU. However, the HPU/CD-Ag nanocomposites displayed better thermal stability with increase in the amount of nanohybrid loading in comparison to both HPU/CD and HPU/Ag (**Table 3.2**).

Table 3.2. Thermal properties of HPU and its nanocomposites

Parameter	HPU	HPU/ Ag	HPU/ CD	HPU/ CD-Ag1	HPU/ CD-Ag2	HPU/ CD-Ag5
Onset temperature (°C)	272	275.2	280.2	286.5	290.6	294.4
1st stage degradation (°C)	371.2	373.3	378.2	382.1	386.4	389.2
2nd stage degradation (°C)	431.5	436.4	439.2	443.3	446.4	449.6
Weight residue (%)	2.7	3.1	3.1	3.4	3.6	3.8
Melting temperature (T_m,°C)	40.2	42.3	43.9	45.2	47.3	49.4
Melting enthalpy (ΔH_m, J g^{-1})	43.5	45.5	46.3	48.13	50.3	54.4

This is attributed to the superior dispersibility of CD-Ag nanohybrid in the HPU matrix and the presence of AgNP which act as the heat stabilizer as well as the nucleating agent for enhancement of the crystallization. The nanohybrid also effectively curbs the movement of the HPU chains [20, 35]. Also, by virtue of large number of functional groups, CD contributes in the physical cross-linking process resulting in effective restrictions in the polymer chain motion and makes the degradation process energy consuming and thereby offering in greater thermo stability of the nanocomposites as compared to HPU. On exposure to thermal energy, the molecular motion and chain excitation are generated which are considerably prohibited due to the secondary interactions of CD with the polymer chains [35]. The enhanced barrier property of the nanocomposites also helps to retain the volatiles produced throughout the decomposition process for a significant time in the matrix and thereby improving the thermal stability. Furthermore the thermal stabilities of the nanocomposites are also enhanced due to the strong covalent and non-covalent interactions between the nanohybrids and HPU matrix.

DSC analyses were conducted to investigate the melting temperature (T_m), melting enthalpy (ΔH_m) and crystallization behavior of HPU nanocomposites as shown in **Figure 3.5d**. It was observed that T_m of the soft segment was evidently reliant on the amount of CD-Ag nanohybrid and shifted to higher temperature with the increase of the nanohybrid content. The presence of nanohybrid restricts the molecular mobility of HPU

chains and thereby enhancing T_m of the nanocomposites [33]. The enhancement of crystallinity can also be predicted from the ΔH_m values as given in **Table 3.2**. The improvement of crystallinity of a semi crystalline polymer on incorporation of various nanomaterials has been reported in relevant literatures [36, 37]. This clearly signifies that the homogenously distributed nanohybrid serves as the nucleating agent and enhances the crystallization process by arranging the soft segment in a particular direction.

3.3.7. Antibacterial activity

Infections associated with surgical implants can lead to severe complications, therefore the prevention of such infections remains a priority [38]. In this context, the prepared films were tested for antibacterial activity. Films containing AgNP exhibited significant antibacterial potency against both the test bacterial strains. The absorbance (λ_{600}) values of cultures containing *S. aureus* and *E. coli* are shown in **Figure 3.6a** and **b**, respectively. The OD of culture in both the bacterial strains increased up to about 90 min indicating growth of bacteria, followed by inhibition in growth around 180 min ($p \leq 0.05$). The decrement continued significantly at 240 min and 300 min ($p \leq 0.01$) in both the cases. The antibacterial activity of the HPU and HPU/CD films was not significant in comparison to the films containing AgNP.

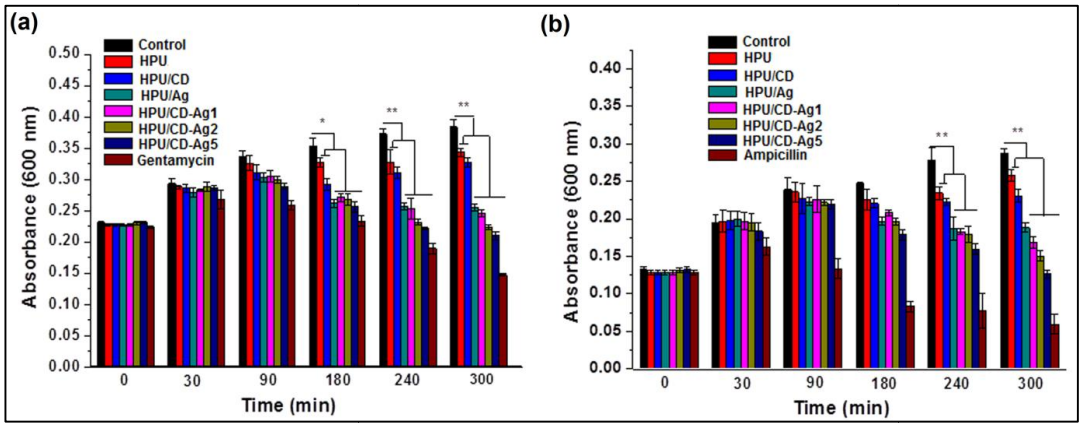

Figure 3.6. Antibacterial activity of the films against **(a)** *E.coli* and **(b)** *S. aureus*. *$p \leq 0.05$, **$p \leq 0.01$.

However, the inhibitory effect of the films was gradual. This may be corroborated with the slow release of AgNP from the film matrix. Literature advocates the antibacterial property AgNP [39]. The HPU/CD-Ag5 (containing the highest amount of AgNP)

exhibited the maximal antibacterial activity ($p \leq 0.01$). The nanocomposite films showed synergistic effect between AgNP and CD for antibacterial activity. The synergistic antibacterial action of AgNP in the presence of carbon based nanomaterials including carbon nanotubes and graphene based quantum dots can have various reasons [40, 41]. The size of the AgNP is an essential factor in their ability to inhibit bacteria. Below an optimum size, bare AgNP exhibit low antibacterial activity, as small sized AgNP are susceptible to formation of microscale clusters. Adhesion of the HPU/CD-Ag nanocomposites to bacterial cellular walls followed by perforation as well as interference of various physiological processes and disruption of gene regulation may be considered as possible reasons for the enhanced antibacterial activity. The synergistic effect may also be an outcome of an effective stabilization (counteraction of aggregation) of AgNP in the presence of CD [41]. Antibiotics- ampicillin and gentamycin were used as positive controls against *S. aureus* and *E. coli* respectively [42]. The inhibition of the bacterial growth could also be assessed by visual turbidity. The culture containing HPU/CD-Ag5 was visually more transparent as compared to others. This study opens up plausible avenue to explore the nanocomposite in stents; however, this demands further *in vivo* assessment. Nevertheless, the results clearly indicate the ability of the HPU/CD-Ag nanocomposites to prevent biofilm formation.

3.3.8. Reduction (%) of bacterial population

The percent reduction of bacterial concentration was determined by normalizing the sample OD value with the control untreated group as shown in **Table 3.3** and **Table 3.4**.

Table 3.3. Reduction (%) of *E. coli*

	90 min	**180 min**	**240 min**	**300 min**
HPU	1.31 ± 0.07	8.55 ± 0.54	15.81 ± 0.59	10.14 ± 0.32
HPU/CD	4.78 ± 0.42	10.63 ± 0.30	20.17 ± 0.44	19.55 ± 0.72
HPU/Ag	6.57 ± 0.14	20.17 ± 0.56	32.90 ± 2.80	34.45 ± 1.06
HPU/CD-Ag1	5.50 ± 0.43	15.65 ±0.28	34.28 ± 0.63	41.50 ± 1.87
HPU/CD-Ag2	7.10 ± 0.10	20.24 ± 0.50	35.58 ± 1.99	47.54 ± 2.16
HPU/CD-Ag5	8.22 ± 0.23	27.50 ± 1.02	42.67 ± 1.74	56.09 ± 2.54
Gentamycin	44.03 ± 4.23	66.21 ± 5.71	72.39 ± 21.75	79.20 ± 16.93

Table 3.4. Reduction (%) of *S. aureus*

	90 min	180 min	240 min	300 min
HPU	3.18 ± 0.11	7.62 ± 0.17	12.08 ± 0.71	10.38 ± 0.20
HPU/CD	7.70 ± 0.30	17.37 ± 0.54	16.69 ± 0.48	14.90 ± 0.34
HPU/Ag	9.86 ± 0.25	26.02 ± 0.64	31.14 ± 0.76	33.46 ± 0.66
HPU/CD-Ag1	9.37 ± 0.27	23.43 ± 0.50	32.07 ± 2.10	36.09 ± 0.81
HPU/CD-Ag2	11.09 ± 0.21	24.27 ± 0.88	38.03 ± 0.74	41.90 ± 0.72
HPU/CD-Ag5	14.09 ± 0.24	27.61 ± 0.83	40.52 ± 0.46	45.15 ± 1.36
Ampicillin	23.09 ± 0.64	33.98 ± 1.28	49.12 ± 2.15	61.63 ± 0.78

The reduction value for the initial time points (*i.e.* 0 min and 30 min) was almost negligible for most of the experimental groups, hence not mentioned in the tables. Polymeric films of HPU/CD-Ag5 were found to exhibit maximal antibacterial activity. The percentages of reduction of bacterial growth for *E. coli* and *S. aureus* were found to be 56.09 ± 2.54% and 45.15 ± 1.36% respectively after 300 min. Thus, the nanocomposite (HPU/CD-Ag5) provides antibacterial activity against *E. Coli.*

3.3.9. Bacterial adhesion test

P. aeruginosa is an opportunistic human pathogen that can colonize the surfaces of stents and frequently linked to infections of indwelling catheters and foreign-body implants [43, 44]. One of the methods by which bacterial colonization can be reduced is the use of medical devices pre-coated or embedded with antimicrobial agents and antiseptics [45]. In this study, the adherence of *P. aeruginosa* to the films was analyzed using FESEM as shown in **Figure 3.7**. The results showed that as compared to the negative control (film without bacterial culture), the films showed a varied response to the bacterial adherence. Maximum bacterial adherence was seen in case of HPU and HPU/CD films covering approximately 70-80% and 50-60% of the films, respectively. The higher bacterial adherence to the HPU and HPU-CD films may be due to the lack of AgNP in it. AgNP have been found to possess antibacterial property [46, 47]. A study by Morones *et al*. showed that AgNP with an average diameter of 21 nm inhibited the growth of Gram-negative bacteria species (*E. coli, Vibrio cholerae, Salmonella typhi*, and *P. aeruginosa*) on agar plates [48]. The HPU/Ag films showed~30-40% bacterial adherence. This 2-fold reduction in adhesion, when compared to HPU might be due to the presence of AgNP in

the films. Lesser bacterial adherence was seen in the nanohybrid films with ~ 20%, ~ 10% and ~ 5% bacterial adherence in HPU/CD-Ag1, HPU/CD-Ag2 and HPU/CD-Ag5 films, respectively. The nanohybrids showed less bacterial adherence in a concentration dependent manner with HPU/CD-Ag5 (containing the highest amount of AgNP) exhibiting least bacterial adherence. A study by Balazs *et al*. reported complete inhibition of bacterial adhesion of *P. aeruginosa* and efficient prevention of colonization using chemically modified (using NaOH and $AgNO_3$ wet treatments) poly(vinyl chloride) for endotracheal tubes [49]. The results of this study were in agreement with that of the antibacterial activity as assessed by the OD method using *E. coli* (Gram negative) and *S. aureus* (Gram positive).

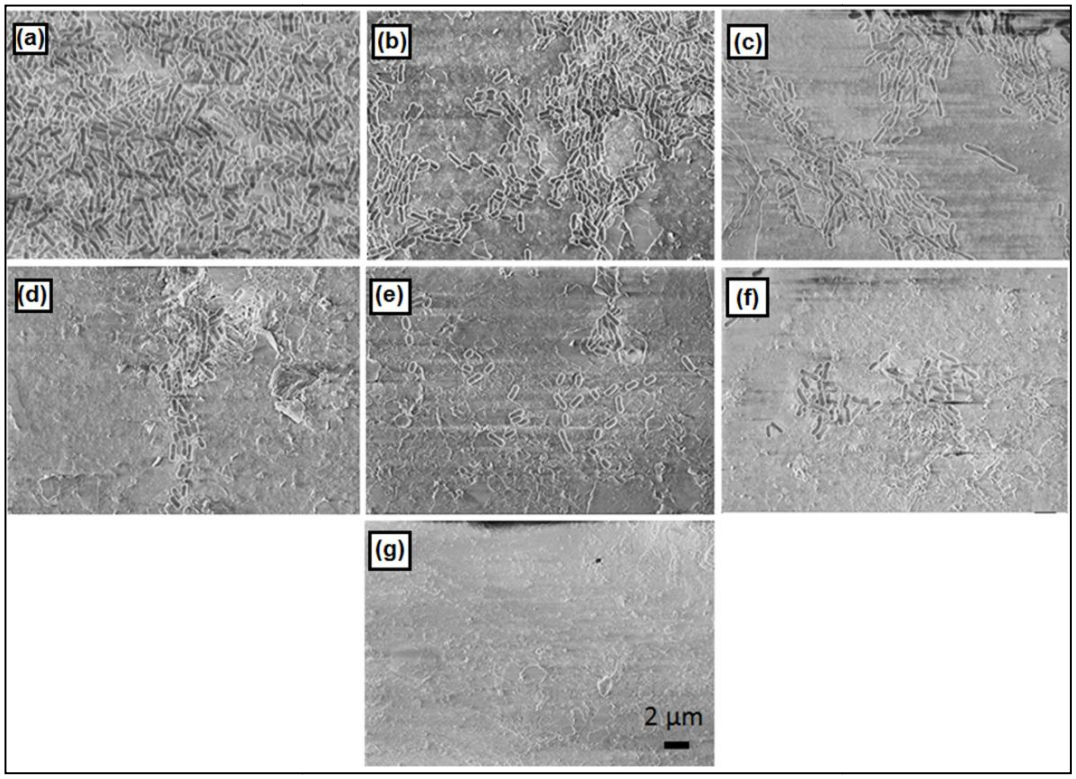

Figure 3.7. Field emission scanning microscopy images of *P. aeruginosa* cultured films **(a)** HPU, **(b)** HPU/CD, (c) HPU-Ag, **(d)** HPU/CD-Ag1, **(e)** HPU/CD-Ag2, **(f)** HPU/CD-Ag5 and **(g)** negative control. Scale bar represents 2 µm.

3.3.10. Platelet attachment, LDH assay and Hemolysis studies

Development of clinically applicable stents demands minimal or no platelet adhesion onto stent material, since they are known to induce thrombogenesis and atherosclerotic

plaque formation [50]. PU in its pristine form exhibits excellent anti-thrombogenicity as attested by several reports [51]. For this purpose the blood compatibility of nanocomposite films was tested. On evaluation under fluorescent microscope, minimal platelet adhesion was observed on HPU nanocomposite films as compared to collagen coated positive control, shown in **Figure 3.8a**. Platelet adhesion was further quantified by measuring the LDH activity which is a direct indication towards adhered activated platelets [22]. Results were in accordance with platelet adhesion test and significantly higher LDH activity compared to different experimental groups was observed for collagen coated surfaces ($p \leq 0.05$) as shown in **Figure 3.8b**. The anti-thrombogenic activity was not altered after nanohybrid incorporation and remained almost same as with pristine HPU films. Compatibility of whole blood with films and their interaction with RBC was analyzed by quantifying RBC lysis [52].

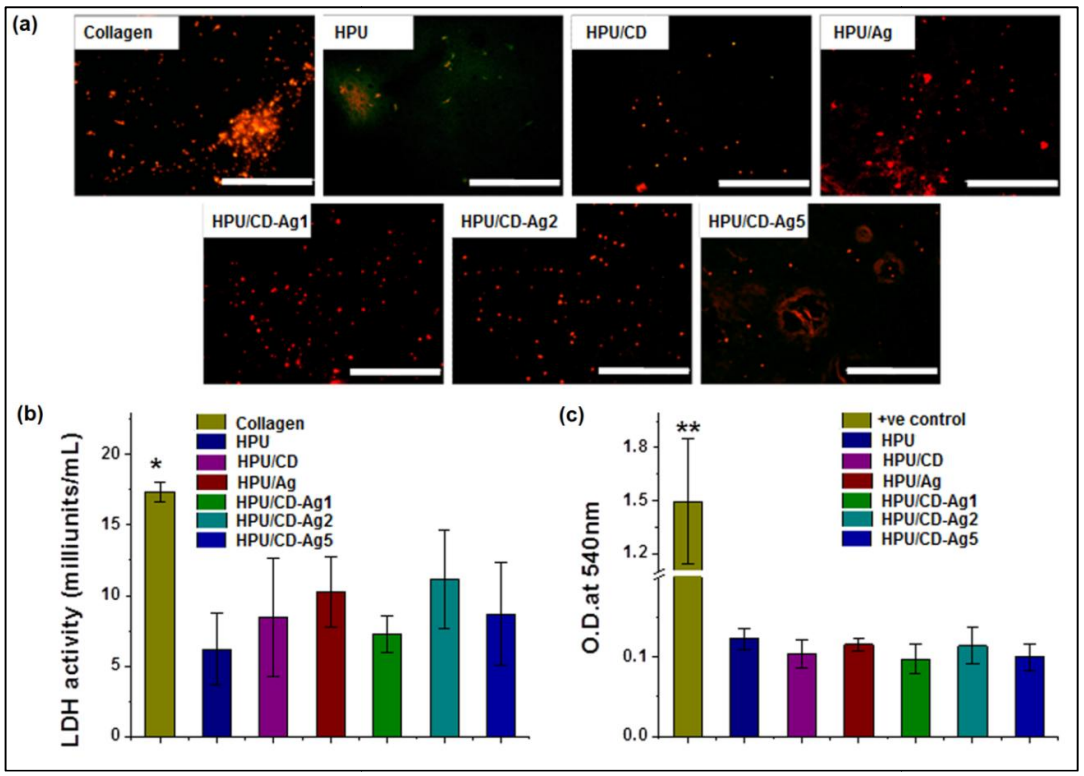

Figure 3.8. *In vitro* blood compatibility of HPU and its nanocomposites. **(a)** Rhodamine phalloidin stained platelets (red color) adhered on to various HPU films after incubation with PRP, **(b)** LDH activity of activated platelets adhered on to various HPU films and **(c)** Quantification of RBC lysis represented in terms of absorbance at 540 nm. *$p \leq 0.05$, **$p \leq 0.01$.

The assay suggested minimal RBC lysis in the blood kept in contact with modified and unmodified HPU films which is comparable with negative control (150 mM NaCl buffer) and significantly lower than positive control (20% TritonX-100) ($p \leq 0.01$) in **Figure 3.8c**. Results suggested no alteration in anti-thrombogenic activity and blood compatibility after incorporating nanohybrid in HPU matrix. Hence these modified HPU films are a suitable candidate for developing stents.

3.3.11. In vitro cytocompatibility of HPU nanocomposites

The SMC and EC are constituents of blood vessel required for vascular functions such as blood pressure control, interactions with immune cells and for uptake of nutrients [53]. Thus, it is imperative to assess the biocompatibility of the films to these cells for their use in biomedical application. The endothelium gets damaged due to implantation of the stent and is repaired by proliferation of SMC [54]. The rate of proliferating SMC is expected to be less than that of EC to avoid restenosis [55]. Thus, a desirable stent should be a better substrate for EC than for SMC. **Figure 3.9a** shows the attachment and morphology of the cells post live/dead staining.

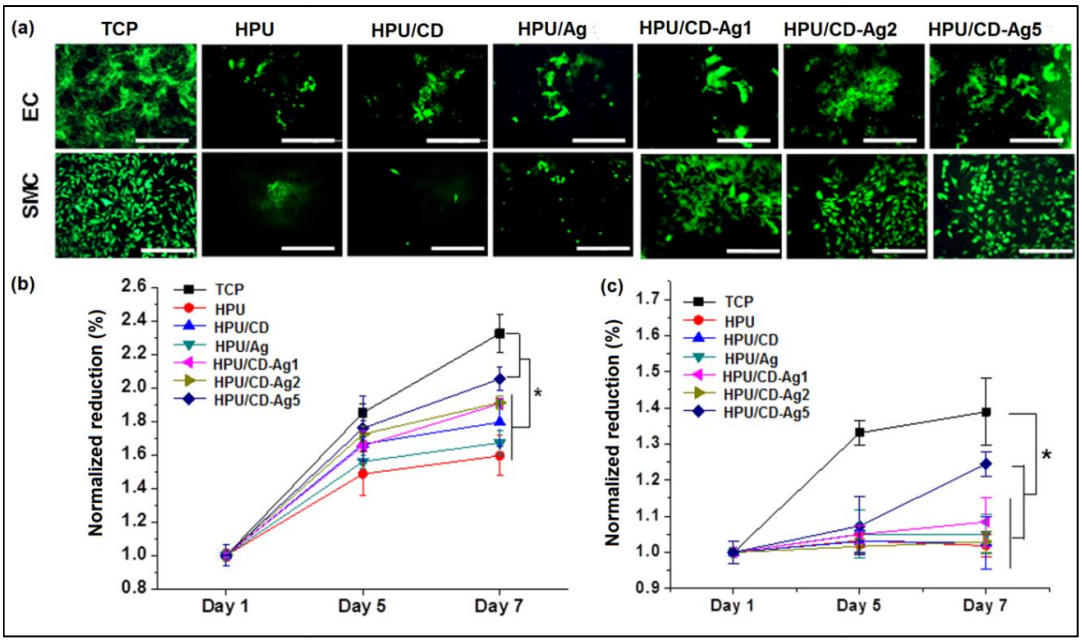

Figure 3.9. *In vitro* cyto-compatability of HPU and its nanocomposites. **(a)** Live-dead images of endothelial cells (EC) and smooth muscle cells (SMC) cultured on films showing cell viability (green color). Proliferation of **(b)** EC and **(c)** SMC at different time points. (*$p \leq 0.05$) Scale bar: 200 µm.

All the films showed cell viability but to a varying degree. In case of EC in **Figure 3.9b**, the HPU, HPU/CD and HPU/Ag films showed lesser viability as compared to HPU/CD-Ag1, HPU/CD-Ag2 and HPU/CD-Ag5. Cells on HPU/CD-Ag5 film showed maximum viability, nearly comparable to that of control TCP. Similar trend was seen in the stained images of SMC, where better viability was assessed on nanocomposite films. However, SMC are more robust and maintain their elongated morphology. This assay shows that these films support cellular viability and proliferation of cells which was further confirmed by performing Alamar Blue assay. As shown in **Figure 3.9b**, the EC showed an increased proliferation in all samples on day 7 as compared to day 1. On day 7, the HPU/CD-Ag films showed higher proliferation rate as compared to the HPU, HPU/CD and HPU/Ag films. Thus, it can be inferred from the results that the HPU/CD-Ag films showed synergistic effect of both AgNP and CD on viability and proliferation of cells by minimizing their cytotoxicity and increasing their biocompatibility [41]. The HPU/CD-Ag5 film showed maximal proliferation among the films and was significantly different from TCP and other samples ($p \leq 0.05$). On the other hand, SMC showed lower proliferation on the films as compared to EC, which is a desirable feature of substrate material to be used as a stent as shown in **Figure 3.9c**. On day 3, there was no significant difference in proliferation among the films seeded with SMC. On day 7, HPU/CD-Ag5 showed lower proliferation than TCP but significantly higher ($p \leq 0.05$) than other films. However, the films other than HPU/CD-Ag5 were not significantly different from each other. The above data suggests that the material is biocompatible and addition of nanohybrid enhances cell viability and proliferation making it good substrates for EC and SMC growth.

3.3.12. Shape memory study

Moreover, HPU and the nanocomposite films exhibited thermal responsive shape-memory behaviors. The shape recovery of the HPU nanocomposites was found to be enhanced with the increase in wt% of nanomaterial (**Table 3.5**). The shape memory effect of SMP is predominantly an entropic process. In the permanent shapes of the HPU nanocomposite and pristine HPU films, the polymeric chains are oriented in a random coil arrangement *i.e.*, at their maximum entropic state. When the nanocomposite films were heated at 70 °C near (~T_m + 20), chain mobility is activated due to which they can be easily distorted into a temporary spiral shape [20, 33, 56].

Table 3.5. Shape memory properties of HPU and its nanocomposites

Property	**HPU**	**HPU/ Ag**	**HPU/ CD**	**HPU/ CD-Ag1**	**HPU/ CD-Ag2**	**HPU/ CD-Ag5**
Shape recovery (%)	98.7 ± 0.1	98.8 ± 0.2	98.9 ± 0.1	99.1 ± 0.2	99.3 ± 0.1	99.6 ± 0.1
Shape fixity (%)	98.6 ± 0.1	98.7 ± 0.2	98.8 ± 0.3	98.8 ± 0.2	99.2 ± 0.1	99.5 ± 0.1
Shape recovery time (s)	20 ± 1	20 ± 1	20 ± 1	20 ± 1	20 ± 1	20 ± 1
Self-expandability (%)	86 ± 0.3	91 ± 0.2	91 ± 0.1	92 ± 0.1	95 ± 0.1	99 ± 0.1
Self-expandability time (s)	25 ± 1	20 ± 1	20 ± 1	20 ± 1	20 ± 1	20 ± 1

Subsequently, when the spirally shaped films were quenched in an ice salt bath, the temporary spiral shape is fixed by kinetic freezing of the polymer's molecular chains and their entropic state is minimized. Once the mechanical stress was removed, the polymeric chains did not have adequate energy to reverse the deformation. Upon immersing the films back into the water at (37 ± 1) °C, the molecular chain mobility was reactivated which allowed the chains to gain entropy and return to the random coil motion. The HPU/CD-Ag5 film exhibited the highest shape recovery among the nanocomposites as shown in **Figure 3.10**, which is higher than most known SMP nanocomposites. Better shape recovery of HPU nanocomposites as compared to HPU is due to the increased stored energy of system due to homogeneous distribution of hard segments, multifunctional moiety hyperbranched polyol, homogenization of reinforcing nanomaterial and increased secondary interactions in the structure of HPU. Thus, the increased stored energy of the homogeneously distributed CD-Ag nanohybrid in the HPU matrix increased the interaction between the CD-Ag nanohybrid and the hard segment of HPU, through generation of strong net points [33]. The CD-Ag nanohybrid helps the nanocomposites to achieve a high recovery stress attributed to the release of the stored elastic strain [20]. The shape recovery of HPU/CD-Ag nanocomposites was found to be enhanced with an increase in amount of nanohybrid in the matrix, which correlates

the improved degree of crystallinity (XRD analysis) to the rising trend of shape recovery [20].

Thus, by deforming such heat sensitive SMPs above their T_m, a desired shape fit can be obtained which can be sustained after cooling. Such SMP nanocomposite can have potential biomedical applications in designing minimally invasive smart implants.

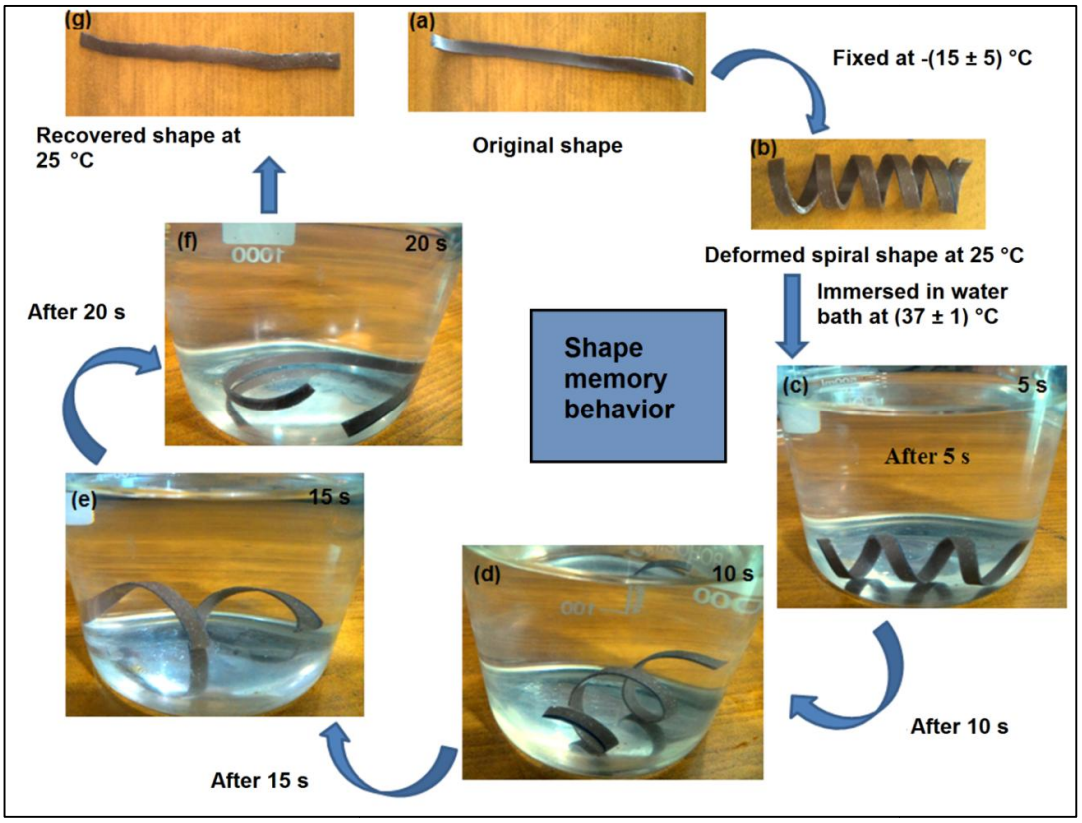

Figure 3.10. Shape-memory effect of HPU/CD-Ag5. **(a)** Original shape, **(b)** temporary fixed spiral shape at 25 °C; shapes after **(c)** 5 s, (d) 10 s and (e) 15 s at (37 ± 1) °C; **(f)** recovered shape after 20 s at (37 ± 1) °C; and **(g)** recovered shape at 25 °C.

3.3.13. Self-expandable study

The rapid expandability rate of HPU/CD-Ag5 is shown in **Figure 3.11**. Self-expandability of stent is highly significant in its use as this property neutralizes the recoil of polymeric stents and serves for an improvement in its anchoring. It is pertinent to mention here that the stent should ideally undergo complete self-expansion to the predetermined diameter within less than a minute. The self-expandability increased significantly with increase in the wt% of nanohybrid in the HPU nanocomposites. All the

HPU nanocomposites showed very good self-expandability within just 20 s, with the HPU/CD-Ag5 film exhibiting the best self-expandability among them. The results also demonstrated good shape fixity at room temperature for all the SMP nanocomposites. The heat absorbing capacity of the nanohybrid generates an increased amount of stored elastic strain energy due to its interactions of the homogeneously distributed nanohybrid with the compatible HPU matrix, mainly by generation of strong net points [20, 33, 56].

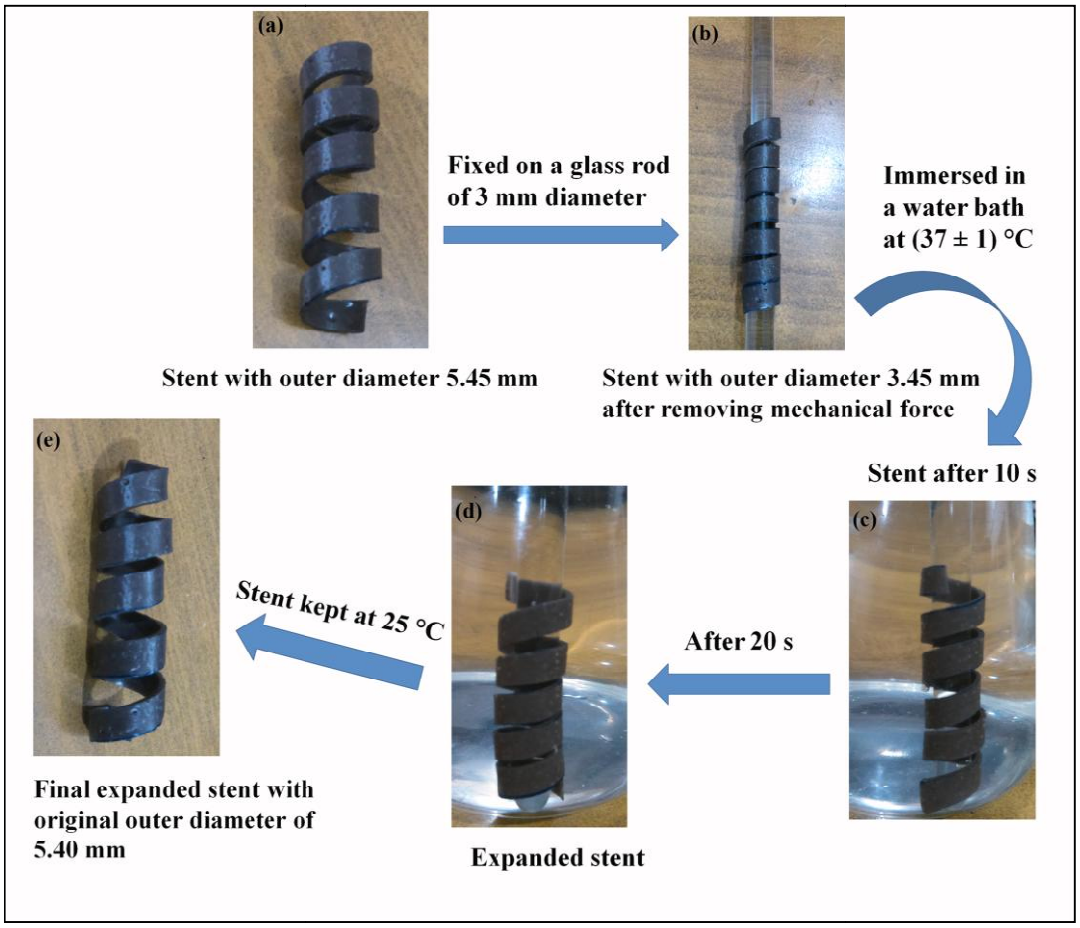

Figure 3.11. Self-expansion behavior of HPU/CD-Ag5 stent. **(a)** Original shape, **(b)** shape after removal of the mechanical force; shapes after **(c)** 10 s and **(d)** 20 s at (37 ± 1) °C; and **(e)** final expanded shape after 20 s at 25 °C.

This assisted the nanocomposite to achieve a higher expandable speed attributed to the release of this stored elastic strain as opposed to that of the pristine HPU. On immersing the HPU/CD-Ag5 stent into water at (37 ± 1) °C, it changed its outer diameter from 3.45 mm to 5.40 mm, within only 20 s which is nearly the full expansion, (**Table 3.5**).

Further, this self-expandable behavior of HPU-CD/Ag5 stent is superior to most known self-expandable polymeric stents [2, 6, 7]. Thus, the novel biodegradable shape memory HPU nanocomposites are potentially functional materials as rapid self-expandable stents.

3.4. Conclusion

Thus, the study demonstrated a facile one-pot single step approach to obtain a carbon dot-silver nanohybrid. An *in situ* fabrication of starch modified hyperbranched polyurethane/carbon dot-silver nanocomposites as rapid self-expandable stents was reported in this chapter. The study witnessed enhanced thermal and mechanical properties and significant shape memory and self-expandable behaviors of the pristine polymer upon formation of nanocomposites by judicious choice of composition and loading of the carbon dot-silver nanohybrid. The nearly complete self-expansion (>99%) of the HPU/CD-Ag5 nanocomposite at (37 ± 1) °C within only 20 s merits special mention as a significant achievement in the present study. The biological assessment particularly antibacterial activity against *Escherichia coli* MTCC 40 and *Staphylococcus aureus* MTCC 3160 bacterial strains confirmed the ability to prevent biofilm formation, and against *Pseudomonas aeruginosa* MTCC 1688 bacterial strain confirmed the ability to prevent bacterial adherence to the fabricated nanocomposites. Further, cell proliferation and differentiation of smooth muscle cells and endothelial cells revealed a cytocompatible material which corroborated its immense prospects in allied biomedical applications. Thus, the simultaneous demonstration of such attractive attributes by a single material justifies the prospects of employing the fabricated nanocomposites to develop rapid self-expandable stents that could overcome the limitations associated with the commonly used conventional stents.

References

[1] Thakur, S. and Karak, N. Multi-stimuli responsive smart elastomeric hyperbranched polyurethane/reduced graphene oxide nanocomposites. *Journal of Materials Chemistry A,* 2(36):14867-14875, 2014.

[2] Xue, L., Dai, S., and Li, Z. Biodegradable shape-memory block co-polymers for fast self-expandable stents. *Biomaterials,* 31(32):8132-8140, 2010.

[3] Nakamura, M., Iwanaga, S., Henmi, C., Arai, K., and Nishiyama, Y. Biomatrices and biomaterials for future developments of bioprinting and biofabrication. *Biofabrication,* 2(1):014110, 2010.

[4] Small, A. J., Coelho-Prabhu, N., and Baron, T. H. Endoscopic placement of self-expandable metal stents for malignant colonic obstruction: long-term outcomes and complication factors. *Gastrointestinal Endoscopy,* 71:560-572, 2010.

[5] Bian, W., Li, D., Lian, Q., Zhang, W., Zhu, L., Li, X., and Jin, Z. Design and fabrication of a novel porous implant with pre-set channels based on ceramic stereolithography for vascular implantation. *Biofabrication*, 3(3):034103, 2011.

[6] Tamai, H., Igaki, K., Kyo, E., Kosuga, K., Kawashima, A., Matsui, S., Komori, H., Tsuji, T., Motohara, S., and Uehata, H. Initial and 6-month results of biodegradable poly-l-lactic acid coronary stents in humans. *Circulation,* 102:399-404, 2000.

[7] Venkatraman, S. S., Tan, L. P., Joso, J. F., Boey, Y. C., and Wang, X. Biodegradable stents with elastic memory. *Biomaterials,* 27(8):1573-1578, 2006.

[8] Lauto, A., Ohebshalom, M., Esposito, M., Mingin, J., Li, P. S., Felsen, D., Goldstein, M., and Poppas, D. P. Self-expandable chitosan stent: design and preparation. *Biomaterials,* 22(13):1869-1874, 2001.

[9] Valimaa, T., Laaksovirta, S., Tammela, T. L. J., Laippala, P., Talja, M., Isotalo, T., Petas, A., Taari, K., and Tormala, P. Viscoelastic memory and self-expansion of self-reinforced bioabsorbable stents. *Biomaterials,* 23(17):3575-3582, 2002.

[10] Das, B., Chattopadhyay, P., Mishra, D., Maiti, T. K., Maji, S., Narayan, R., and Karak, N. Nanocomposites of bio-based hyperbranched polyurethane/funtionalized MWCNT as nonimmunogenic, osteoconductive, biodegradable and biocompatible scaffolds in bone tissue engineering. *Journal of Materials Chemistry B,* 1(33):4115-4126, 2013.

[11] Mauter, M. S. and Elimelech, M. Environmental applications of carbon-based nanomaterials. *Environmental Science & Technology,* 42(16):5843-5859, 2008.

[12] Du, F., Zhang, M., Li, X., Li, J., Jiang, X., Li, Z., Hua, Y., Shao, G., Jin, J., and Shao, Q. Economical and green synthesis of bagasse-derived fluorescent carbon dots for biomedical applications. *Nanotechnology*, 25(31):315702, 2014.

[13] Li, S., Guo, Z., Zhang, Y., Xue, W., and Liu, Z. Blood compatibility evaluations of fluorescent carbon dots. *ACS Applied Materials and Interfaces,* 7(34):19153-19162, 2015.

[14] Pavithra, D. and Doble, M. Biofilm formation, bacterial adhesion and host response on polymeric implants-issues and prevention. *Biomedical Materials*, 3(3):034003, 2008.

[15] Gwon, D. I., Lee, S. S., and Kim, E. Y. Cefotaxime-eluting covered self-expandable stents in a canine biliary model: scanning electron microscopic study of biofilm formation. *Acta Radiologica,* 53(10):1127-1132, 2012.

[16] Castellano, J. J., Shafii, S. M., Ko, F., Donate, G., Wright, T. E., Mannari, R. J., Payne, W. G., Smith, D. J., and Robson, M. C. Comparative evaluation of silver-containing antimicrobial dressings and drugs. *International Wound Journal,* 4(2):114-122, 2007.

[17] Richard, J. W., Spencer, B. A., McCoy, L. F., Carina, E., Washington, J., and Edgar, P. Acticoat versus silverion: the truth. *Journal of Burn Care & Rehabilitation,* 1(1):11-20, 2002.

[18] Wen, W., Ma, L. M., He, W., Tang, X. W., Zhang, Y., Wang, X., Liu, L., and Fan, Z. N. Silver-nanoparticle-coated biliary stent inhibits bacterial adhesion in bacterial cholangitis in swine. *Hepatobiliary & Pancreatic Diseases International,* 15(1):87-92, 2016.

[19] Yang, F., Ren, Z., Chai, Q., Cui, G., Jiang, L., Chen, H., Feng, Z., Chen, X., Ji, J., Zhou, L., Wang, W., and Zheng, S. A novel biliary stent coated with silver nanoparticles prolongs the unobstructed period and survival via anti-bacterial activity. *Scientific Reports*, 2016, DOI: 10.1038/srep21714.

[20] Thakur, S. and Karak, N. Bio-based tough hyperbranched polyurethane-graphene oxide nanocomposites as advanced shape memory materials. *RSC Adv*ances, 3(24):9476-9482, 2013.

[21] Lendlein, A., Jiang, H. Y., Junger, O., and Langer, R. Light-induced shape-memory polymers. *Nature*, 434:879-882, 2005.

[22] Cutiongco, M. F., Anderson, D. E., Hinds, M. T., and Yim, E. K. *In vitro* and *ex vivo* hemocompatibility of off-the-shelf modified poly (vinyl alcohol) vascular grafts. *Acta biomaterialia,* 25:97-108, 2015.

[23] Evans, B. C., Nelson, C. E., Yu, S. S., Beavers, K. R., Kim, A. J., Li, H., Nelson, H. M., Giorgio, T. D., and Duvall, C. L. *Ex vivo* red blood cell hemolysis assay for the evaluation of pH-responsive endosomolytic agents for cytosolic delivery of biomacromolecular drugs. *Journal of Visualized Experiments: JoVE*, 73:50166, 2013.

[24] Butcher, J. T. and Nerem, R. M. Porcine aortic valve interstitial cells in three-dimensional culture: comparison of phenotype with aortic smooth muscle cells. *Journal of Heart Valve Disease,* 13(3):478-486, 2004.

[25] De, B., Kumar, M., Mandal, B. B., and Karak. N. An *in situ* prepared photo-luminescent transparent biocompatible hyperbranched epoxy/carbon dot nanocomposite. *RSC Advances,* 5(91):74692-74704, 2015.

[26] Sk, M. P., Jaiswal, A., Paul, A., Ghosh, S. S., and Chattopadhyay, A. Presence of amorphous carbon nanoparticles in food caramels. *Scientific Reports,* 2:383, 2012.

[27] Gogoi, S., Kumar, M., Mandal, B. B., and Karak, N. High performance luminescent thermosetting waterborne hyperbranched polyurethane/carbon quantum dot nanocomposite with in vitro cytocompatibility. *Composites Science Technol*ogy, 118:39-46, 2015.

[28] Sahu, S., Behera, B., Maiti, T. K., and Mohapatra, S. Simple one-step synthesis of highly luminescent carbon dots from orange juice: application as excellent bio-imaging agents. *Chemical Communications,* 48(70):8835-8837, 2012.

[29] Falco, C., Baccile, N., and Titirici, M. M. Morphological and structural differences between glucose, cellulose and lignocellulosic biomass derived hydrothermal carbons. *Green Chem*istry, 13(11):3273-3281, 2011.

[30] Ryu, J. Y., Suh, W., Suh, D. J., and Ahn, D. J. Hydrothermal preparation of carbon microspheres from mono-saccharides and phenolic compounds. *Carbon,* 48(7):1990-1998, 2010.

[31] De, B. and Karak, N. A green and facile approach for the synthesis of water soluble fluorescent carbon dots from banana juice. *RSC Advances,* 3(22):8286-8290, 2013.

[32] Gupta, K., Barua, S., Hazarika, S. N., Manhar, A. K., Nath, D., Karak, N., Namsa, N. D., Mukhopadhyay, R., Kalia, V. C., and Mandal, M. Green silver nanoparticles: enhanced antimicrobial and antibiofilm activity with effects on DNA replication and cell cytotoxicity, *RSC Advances*, 4(95):52845-52855, 2014.

[33] Thakur, S. and Karak, N. A tough smart elastomeric bio-based hyperbranched polyurethane nanocomposite. *New Journal of Chemistry*, 39(3):2146-2154, 2015.

[34] Deka, H., Karak, N., Kalita, R. D., and Buragohain, A. K. Bio-based thermostable, biodegradable and biocompatible hyperbranched polyurethane/Ag

nanocomposites with antimicrobial activity. *Polymer Degradation and Stability*, 95(9):1509-1517, 2010.

[35] Zhao, X., Zhang, Z., Wang, L., Xi, K., Cao, Q., Wang, D., Yang, Y., and Du, Y. Excellent microwave absorption property of graphene-coated Fe nanocomposites. *Scientific Rep*orts, 3:3421, 2013.

[36] Karak, N., Konwarh, R., and Voit, B. Catalytically active vegetable-oil-based thermoplastic hyperbranched polyurethane/silver nanocomposites. *Macromolecular Materials and Engineering,* 295(2):159-169, 2010.

[37] Tzavalas, S., Mouzakis, D. E., Drakonakis, V., and Gregoriou, V. G. Polyethylene terephthalate-multiwall nanotubes nanocomposites: effect of nanotubes on the conformations, crystallinity and crystallization behavior of PET. *Journal of Polymer Science Part B: Polymer Physics*, 46(7):668-76, 2008.

[38] Darouiche R. O. Antimicrobial approaches for preventing infections associated with surgical implants. *Clinical Infectious Diseases,* 36(10):1284-89, 2003.

[39] Guzman, M., Dille, J., and Godet, S. Synthesis and antibacterial activity of silver nanoparticles against gram-positive and gram-negative bacteria. *Nanomedicine: Nanotechnology, Biology and Medicine,* 8(1):37-45, 2012.

[40] Kazmi, S. J., Shehzad, M., Mehmood, S., Yasar, M., Naeem, A. and Bhatti, A. Effect of varied Ag nanoparticles functionalized CNTs on its anti-bacterial activity against *E. coli*. *Sensors and Actuators A: Physical*, 216:287-924, 2014.

[41] Habiba, K., Bracho-Rincon, D. P., Gonzalez-Feliciano, J. A., Villalobos-Santos, J. C., Makarov, V. I., Ortiz, D., Avalos, J. A., Gonzalez, C. I., Weiner, B. R., and Morell, G.. Synergistic antibacterial activity of PEGylated silver-graphene quantum dots nanocomposites. *Applied Materials Today,* 1(2):80-87, 2015.

[42] Barua, S., Konwarh, R., Bhattacharya, S. S., Das, P., Devi, K. S. P., Maiti, T. K., Mandal, M., and Karak, N. Non-hazardous anticancerous and antibacterial colloidal 'green' silver nanoparticles. *Colloids and Surfaces B: Biointerfaces*, 105:37-42, 2013.

[43] Kerr, K. G. and Snelling, A. M. *Pseudomonas aeruginosa*: a formidable and ever-present adversary. *Journal of Hospital Infection,* 73(4):338-344, 2009.

[44] Brouqui, P., Rousseau, M. C., Stein, A., Drancourt, M., and Raoult, D. Treatment of Pseudomonas aeruginosa-infected orthopedic prostheses with ceftazidime-ciprofloxacin antibiotic combination. *Antimicrobial Agents and Chemotherapy*, 39(11):2423-2425, 1995.

[45] Hall-Stoodley, L., Costerton, J. W., and Stoodley, P. Bacterial biofilms: from the natural environment to infectious diseases. *Nature Reviews Microbiology,* 2(2):95-108, 2004.

[46] Franci, G., Falanga, A., Galdiero, S., Palomba, L., Rai, M., Morelli, G., and Galdiero, M. Silver nanoparticles as potential antibacterial agents. *Molecules*, 20(5):8856-8874, 2015.

[47] Kim, J. S., Kuk, E., Yu, K. N., Kim, J. H. Park, S. J., Lee, H. J., Kim, S. H., Park, Y. K., Park, Y. H., Hwang, C. Y., Kim, Y. K., Lee, Y. S., Jeong, D. H., and Cho, M. H. Antimicrobial effects of silver nanoparticles. *Nanomedicine*, 3(1):95-101, 2007.

[48] Morones, J. R., Elechiguerra, J. L., Camacho, A., Holt, K., Kouri, J. B., Ramírez, J. T., and Yacaman, M. J. The bactericidal effect of silver nanoparticles. *Nanotechnology,* 16(10):2346-2353, 2005.

[49] Balazs, D. J., Triandafillu, K., Chevolot, Y., Aronsson, B. O., Harms, H., Descouts, P., and Mathieu, H. J. Surface modification of PVC endotracheal tubes by oxygen glow discharge to reduce bacterial adhesion. *Surface and Interface Analysis*, 35(3):301-309, 2003.

[50] Packham, M. A. Role of platelets in thrombosis and hemostasis. *Canadian Journal of Physiology and Pharmacology,* 72(3):278-284, 1994.

[51] Das, B., Mandal, M., Upadhyay, A., Chattopadhyay, P., and Karak, N. Bio-based hyperbranched polyurethane/Fe_3O_4 nanocomposites: smart antibacterial biomaterials for biomedical devices and implants. *Biomedical Materials,* 8(3):035003, 2013.

[52] Barua, S., Das, G., Aidew, L., Buragohain, A. K., and Karak, N. Copper-copper oxide coated nanofibrillar cellulose: a promising biomaterial. *RSC Advances,* 3(35):14997-15004, 2013.

[53] Patsch, C., Challet-Meylan, L., Thoma, E. C. Urich, E., Heckel, T., O'Sullivan, J. F., Grainger, S. J., Kapp, F. G., Sun, L., Christensen, K., Xia, Y., Florido, M. H. C., He, W., Pan, W., Prummer, M., Warren, C. R., Jakob-Roetne, R., Certa, U., Jagasia, R., Freskgård, P. O., Adatto, I., Kling, D., Huang, P., Zon, L. I., Chaikof, E. L., Gerszten, R. E., Graf, M., Iacone, R., and Cowan, C. A. Generation of vascular endothelial and smooth muscle cells from human pluripotent stem cells. *Nature Cell Biology*, 17:994-1003, 2015.

[54] Serrano, M. C., Portolés, M. T., Vallet-Regí, M., Izquierdo, I., Galletti, L., Comas, J. V., and Pagani, R. Vascular endothelial and smooth muscle cell culture on NaOH-treated poly(ε-caprolactone) films: a preliminary study for vascular graft development. *Macromolecular Bioscience,* 5(5):415-423, 2005.

[55] Jing, F. J., Huang, N., Wang, L., Fu, R. K. Y., Mei, Y. F., Leng, Y. X., Chen, J. Y., Liu, X. Y., and Chu, P. K. Behavior of human umbilical vein endothelial cells on micro-patterned amorphous hydrogenated carbon films produced by plasma immersion ion implantation and deposition & plasma etching. *Diamond and Related Materials,* 16(3):550-557, 2007.

[56] Mya, K. Y., Gose, H. B., Pretsch, T., Bothe, M., and He, C. Star-shaped POSS-polycaprolactone polyurethanes and their shape memory performance. *Journal of Materials Chemistry*, 21(13):4827-4836, 2011.